



# H $\alpha$ Emission and H II Regions at the Locations of Recent Supernovae in Nearby Galaxies

Ness Mayker Chen<sup>1,2</sup>, Adam K. Leroy<sup>1,2</sup>, Sumit K. Sarbadhicary<sup>1,2</sup>, Laura A. Lopez<sup>1,2</sup>, Todd A. Thompson<sup>1,2</sup>, Ashley T. Barnes<sup>3</sup>, Eric Emsellem<sup>4,5</sup>, Brent Groves<sup>6</sup>, Rupali Chandar<sup>7</sup>, Mélanie Chevance<sup>8,9,19</sup>, Ryan Chown<sup>1</sup>, Daniel A. Dale<sup>10</sup>, Oleg V. Egorov<sup>11</sup>, Simon C. O. Glover<sup>8</sup>, Kathryn Grasha<sup>12,20</sup>, Ralf S. Klessen<sup>8,13</sup>, Kathryn Kreckel<sup>11</sup>, Jing Li<sup>11</sup>, J. Eduardo Méndez-Delgado<sup>11</sup>, Eric J. Murphy<sup>14</sup>, Debosmita Pathak<sup>1,2</sup>, Eva Schinnerer<sup>15</sup>, David A. Thilker<sup>16</sup>, Leonardo Úbeda<sup>17</sup>, and Thomas G. Williams<sup>18</sup>

<sup>1</sup> Department of Astronomy, The Ohio State University, 140 West 18th Avenue, Columbus, OH 43210, USA; [maykerchen.1@osu.edu](mailto:maykerchen.1@osu.edu)

<sup>2</sup> Center for Cosmology and Astroparticle Physics, 191 West Woodruff Avenue, Columbus, OH 43210, USA

<sup>3</sup> European Southern Observatory, Karl-Schwarzschild Straße 2, D-85748 Garching bei München, Germany

<sup>4</sup> European Southern Observatory, Karl-Schwarzschild-Straße 2, 85748 Garching, Germany

<sup>5</sup> Univ Lyon, Univ Lyon1, ENS de Lyon, CNRS, Centre de Recherche Astrophysique de Lyon UMR5574, F-69230 Saint-Genis-Laval, France

<sup>6</sup> International Centre for Radio Astronomy Research, University of Western Australia, 7 Fairway, Crawley, 6009 WA, Australia

<sup>7</sup> Ritter Astrophysical Research Center, University of Toledo, Toledo, OH 43606, USA

<sup>8</sup> Universität Heidelberg, Zentrum für Theoretische Astrophysik, Albert-Ueberle-Str 2, D-69120 Heidelberg, Germany

<sup>9</sup> Cosmic Origins Of Life (COOL) Research DAO, Germany

<sup>10</sup> Department of Physics and Astronomy, University of Wyoming, Laramie, WY 82071, USA

<sup>11</sup> Astronomisches Rechen-Institut, Zentrum für Astronomie der Universität Heidelberg, Mönchhofstraße 12-14, D-69120 Heidelberg, Germany

<sup>12</sup> Research School of Astronomy and Astrophysics, Australian National University, Canberra, ACT 2611, Australia

<sup>13</sup> Universität Heidelberg, Interdisziplinäres Zentrum für Wissenschaftliches Rechnen, Im Neuenheimer Feld 205, D-69120 Heidelberg, Germany

<sup>14</sup> National Radio Astronomy Observatory, 520 Edgemont Road, Charlottesville, VA 22903-2475, USA

<sup>15</sup> Max-Planck-Institut für Astronomie, Königstuhl 17, D-69117, Heidelberg, Germany

<sup>16</sup> Center for Astrophysical Sciences, Johns Hopkins University, Baltimore, MD 21218, USA

<sup>17</sup> Space Telescope Science Institute, Baltimore, MD, USA

<sup>18</sup> Subdepartment of Astrophysics, Department of Physics, University of Oxford, Keble Road, Oxford OX1 3RH, UK

Received 2024 March 30; accepted 2024 April 15; published 2024 June 18

## Abstract

We present a statistical analysis of the local,  $\approx 50$ – $100$  pc scale, H $\alpha$  emission at the locations of recent ( $\leq 125$  yr) supernovae (SNe) in nearby star-forming galaxies. Our sample consists of 32 SNe in 10 galaxies that are targets of the PHANGS-MUSE survey. We find that 41% (13/32) of these SNe occur coincident with a previously identified H II region. For comparison, H II regions cover 32% of the area within  $\pm 1$  kpc of any recent SN. Contrasting this local covering fraction with the fraction of SNe coincident with H II regions, we find a statistical excess of  $7.6\% \pm 8.7\%$  of all SNe to be associated with H II regions. This increases to an excess of  $19.2\% \pm 10.4\%$  when considering only core-collapse SNe (CCSNe). These estimates appear to be in good agreement with qualitative results from new, higher-resolution Hubble Space Telescope H $\alpha$  imaging, which also suggests many CCSNe detonate near but not in H II regions. Our results appear consistent with the expectation that only a modest fraction of stars explode during the first  $\lesssim 5$  Myr of the life of a stellar population when H $\alpha$  emission is expected to be bright. Of the H II region associated SNe, 85% (11/13) also have associated detected CO(2–1) emission, indicating the presence of molecular gas. The SNe associated with H II regions have typical extinctions of  $A_V \sim 1$  mag, consistent with a significant amount of pre-clearing of gas from the region before the SNe explode.

*Unified Astronomy Thesaurus concepts:* Supernovae (1668); Core-collapse supernovae (304); H II regions (694); Star forming regions (1565); Stellar feedback (1602); Galaxy evolution (594)

## 1. Introduction

In this paper, we leverage new, high-physical-resolution, high-sensitivity maps of H $\alpha$  emission from nearby galaxies to assess the coincidence between recent supernovae (SNe) and H II regions. This measurement can help constrain both the nature of SN progenitors and the environments into which SNe explode.

Bright regions of H $\alpha$  emission in galaxies are indicative of H II regions, where short-lived ( $\lesssim 5$  Myr), massive ( $> 10 M_{\odot}$ )

stars ionize the gas through photons with energies higher than 13.6 eV. Therefore we would expect SNe in close proximity to H II regions to likely originate from massive, short-lived progenitors. Such proximity studies have been particularly useful for understanding if and how the different subtypes of core-collapse SNe (CCSNe), Types II, Ib, and Ic, correspond to different progenitor mass and age ranges (e.g., Anderson et al. 2015b), something that has been challenging to infer from direct photometry/spectroscopic observations of the SNe (e.g., Dessart & Hillier 2022).

SN environment studies attempt to constrain the delay time and progenitor populations for SNe by measuring the correlation of the different SN types with various stellar populations and tracers of star formation (see Anderson et al. 2015b, for an excellent review). In a key early study, van Dyk et al. (1996) found  $\sim 70\%$  of CCSNe to be associated with H II regions. More recently, Audcent-Ross et al. (2020) compared

<sup>19</sup> [coolresearch.io](https://coolresearch.io)

<sup>20</sup> ARC DECRA Fellow.

the radial distributions of 80 SNe with  $R$ -band, UV, and  $H\alpha$  emissions in the SINGG/SUNGG galaxy surveys. They found SNe Ia correlated with  $R$ -band light, an indicator of the presence of low-mass progenitors; SNe II were correlated with far-ultraviolet emission, consistent with moderately massive progenitors; and stripped-enveloped SNe (SESNe) were found to be the most associated with  $H\alpha$  emission, suggestive of SESNe originating from the most massive progenitor systems. Recent studies expanded beyond only imaging to also leverage integral-field-unit data (e.g., Anderson 2014; Galbany et al. 2017). These studies consistently show that SNe Ia (white dwarf SNe) are the most weakly associated with tracers of star formation and instead associated with the older stellar population (e.g., Pritchett et al. 2024). SNe Ib/c (stripped-envelope core-collapse SNe) are more associated with tracers of very recent star formation than SNe II (other core-collapse SNe; Crowther 2013; Galbany et al. 2014) but with subtle differences between SNe Ib and Ic (James & Anderson 2006; Anderson et al. 2012). These results support a picture with an increasing progenitor mass sequence, SNe Ia  $\rightarrow$  SNe II  $\rightarrow$  SNe Ib  $\rightarrow$  SNe Ic (but note that binary evolution can have a complicating effect on this simple picture; e.g., Kuncarayakti et al. 2013; Zapartas et al. 2017).

The coincidence (or not) of SNe and H II regions also has significant implications for the mechanisms and impact of stellar feedback in various contexts. A variety of observational evidence supports that cold, molecular gas is often substantially cleared from a star-forming region *before*  $H\alpha$  fades (e.g., Schruha et al. 2010; Kruijssen et al. 2019; Schinnerer et al. 2019; Chevance et al. 2020; Kim et al. 2022; Pan et al. 2022). Measurements of resolved  $H\alpha$  emission around clusters with spectral energy distribution modeling-based ages also suggest that the ionized gas may be cleared on a few Myr timescales, even before ionizing photon production stops (e.g., Hannon et al. 2022). If SNe have an important role in this rapid gas clearing, then they must be present to some degree within H II regions. Arguments based on stellar evolution timescales ascribed most of this gas clearing to “pre-SN” feedback: stellar winds, radiation pressure, and ionized gas pressure (e.g., Lopez et al. 2014; McLeod et al. 2019, 2020, 2021; Barnes et al. 2020, 2022; Olivier et al. 2021; Chevance et al. 2022). Directly measuring the coincidence of SNe with H II regions provides an independent, empirical test.

Conversely, SNe explosions in galaxy disks are important to supporting the overall gas disk, launching galactic winds, and stirring turbulence (e.g., Elmegreen 2004; Ostriker & Shetty 2011; Walch et al. 2015; Girichidis et al. 2016; Veilleux et al. 2020). The environment where a SN explodes has a significant impact on its zone of influence, with explosions in denser environments exerting a more local influence both because the high density leads to a shorter cooling time and because the momentum injected by the supernova affects a smaller physical region at high density (e.g., Walch et al. 2015; Gatto et al. 2017; Keller & Kruijssen 2020). Away from the dense gas of star-forming regions, SN explosions are free to impact a larger area and exert this “large-scale” feedback (e.g., Barnes et al. 2023). Therefore demonstrating what fraction of these explosions in fact do occur away from dense gas represents an important avenue to quantitatively understand feedback in stellar disks. Recently both Mayker Chen et al. (2023) and Sarbadhicary et al. (2023) measured the cold gas content (CO and H I) at the sites of recent SNe or likely near-

future SNe in nearby galaxies. They found evidence for substantial populations of SNe away from CO emission and well-positioned to explode into low-density regions. Even SNe close to star-forming regions of galaxies can still go off in the low-density environments found in bubbles carved out by stellar populations and previous SNe (Bagetakos et al. 2011; Pokhrel et al. 2020; Barnes et al. 2023; Egorov et al. 2023; Watkins et al. 2023a, 2023b).

Because SNe are rare, SN environment studies have often been forced to work with samples of distant objects with relatively coarse physical resolution. This can make it difficult to distinguish cases where an SN occurs *within* an H II region from cases in which the SN only occurs *near* the H II region. Studies at higher resolution are needed to directly measure the fraction of SNe that are actually occurring *within* H II regions and to place these explosions accurately within the multiphase interstellar medium (ISM).

In this work, we adopt a slightly different approach compared to these earlier studies. While they often characterize the sites of SN explosions after detecting them, we instead focus on identifying SNe and determining their locations within a uniquely well-studied set of nearby  $\lesssim 20$  Mpc galaxies, the PHANGS surveys (Leroy et al. 2021; Emsellem et al. 2022; Lee et al. 2022). Because PHANGS targets very nearby galaxies, even seeing-limited ground-based observations achieve a physical resolution of  $\lesssim 100$  pc, up to 10 times sharper than previous studies. This offers the prospect to better localize SNe relative to H II regions, and from the rich supporting data, we can construct a variety of careful controls using data at other wavelengths. This high physical resolution and multiwavelength coverage offers the prospect to “zoom in” on individual SN sites to directly see the likely area of influence of the SN and so understand its future impact.

We took the first step toward this goal of characterizing the local sites of SNe in Mayker Chen et al. (2023), where we studied the CO (2–1) emission from SNe in the PHANGS–Atacama Large Millimeter/submillimeter Array (ALMA) survey (Leroy et al. 2021). In this paper, we take the next logical step: comparing SNe to tracers of the ionized gas and young, massive stars using the PHANGS–Multi-Unit Spectroscopic Explorer (MUSE) survey (Emsellem et al. 2022) and including a first look based on the PHANGS– $H\alpha$  Hubble Space Telescope (HST) survey (P.I. R. Chandar; Chandar, A. Barnes et al. 2024, in preparation; Barnes et al. 2022). PHANGS–MUSE, our core comparison data set, provided spectroscopic optical mapping at  $\lesssim 1''$  resolution for 19 galaxies. This includes high-quality maps of  $H\alpha$  and  $H\beta$  (e.g., Belfiore et al. 2022, 2023) that have been used to identify and characterize  $\sim 20,000$  individual nebular regions (Groves et al. 2023). We identify 32 SNe that have occurred within 10 targets of PHANGS–MUSE and characterize their explosion sites, exploring implications for SN progenitors and stellar feedback.

In Section 2 we describe our experimental design and data. In Section 2.1 we summarize the data used in this work. In Section 2.2 we discuss how our SN sample is compiled. In Section 2.3 we discuss the control measurements that we make to help interpret our results. In Section 3 we report on the  $H\alpha$  emission at our SN sites. In Section 3.1 we measure the fraction of SN sites coincident with an H II region; in Section 3.2 we analyze our SN population by type; in Section 3.3 we compare our findings with expectations of simple stellar population (SSP) models; in Section 3.4 we compare the distance to the

nearest H II region from our real SN sample to three model populations of SNe; in Section 3.5 we compare the distributions of H $\alpha$  emission present at the sites of the real SNe to our model populations; and then in Section 3.6 we zoom in to examine the local MUSE and HST H $\alpha$  emission from our SN sites. In Section 4 we also consider other properties of the ISM at the sites of our SN sample. In Section 4.1 we look at how the incidence of molecular gas relates to the presence of H II regions; in Section 4.2 we compare the extinction at each of our SN sites to that of the host galaxies overall; and in Section 4.3 we report additional diagnostics at each of our SN sites, including velocity dispersion, metallicity, and BPT classifications. Finally, in Section 5 we summarize and discuss our results.

## 2. Methods

### 2.1. Data

The PHANGS–MUSE survey (Emsellem et al. 2022) mapped 19 nearby, star-forming galaxies (distances  $<20$  Mpc, inclinations  $<60^\circ$ ) using the MUSE instrument (Bacon et al. 2010) on the ESO Very Large Telescope (VLT). For this work, we use attenuation-corrected H $\alpha$  emission maps (see Figures 1 and 2) produced by Belfiore et al. (2023; see also Pessa et al. 2021). We use the “copt” convolved and optimized standard products. These have resolution that varies from galaxy to galaxy ranging between  $0''.78$  and  $1''.25$ , which translates to linear resolution of 33–104 pc at the distance of our targets (see Table A2). The MUSE astrometry is calibrated against Gaia via a procedure detailed in Emsellem et al. (2022) and so is expected to be accurate to within a few tenths of an arcsecond.

The MUSE maps have high signal-to-noise ratios, recovering H $\alpha$  emission almost everywhere. Emsellem et al. 2022 found that more than 95% of  $0''.2$  spaxels within  $0.5 R_{25}$  contain H $\alpha$  emission at a  $3\sigma$  level. However, much of this emission represents diffuse ionized gas, likely powered by photons leaked from H II regions (e.g., Belfiore et al. 2022). To distinguish likely actual H II regions from this extended emission, we use the PHANGS nebular catalog (Santoro et al. 2022; Groves et al. 2023) to determine where there is an H II region along the line of sight. These H II regions are identified using the HIIPhot algorithm (Thilker et al. 2000) adopting a single termination gradient of the H $\alpha$  surface brightness. For more information, see Section 3.1 of Groves et al. (2023).

In Table A2, we report the nebular catalog’s BPT flags for three emission line diagnostics, [N II]  $\lambda 6584$ , [S II]  $\lambda 6717$ , and [O I]  $\lambda 6300$  (for more information, see Section 4.2 of Groves et al. 2023). These diagnostics help determine whether the emission is more likely to arise from an H II region or another type of nebula, e.g., supernova remnant shocks, winds, or planetary nebulae. As we discuss further in Section 4.3, all 13 SNe that are within the line of sight of nebular emission show diagnostics suggesting that the nebular emission is caused by star formation, and all have low H $\alpha$  velocity dispersions. Overall, the H $\alpha$  emission occurring within the line of sight to our SN sample is consistent with emission from H II regions. Because our sample consists of young SNe, we do not expect that they have had time to influence their environment and the BPT diagnostics are unlikely to be affected by the SNe themselves. The one exception is SN2017gax which was observed by PHANGS–MUSE shortly after the SN and

contains the spectrum of the explosion. As a result, we remove this object from our sample.

In addition to the MUSE data, we compare SN locations to new narrowband H $\alpha$  emission maps from the HST (P.I. R. Chandar; R. Chandar, A. Barnes et al. 2024, in preparation). These are similar to the map of NGC 1672 presented in Barnes et al. (2022) with similar processing applied. Because they are diffraction-limited at  $\approx 0''.1$  resolution (2.6–9 pc linear resolution), they offer a much sharper view of H $\alpha$  emission and H II regions than VLT–MUSE but with worse surface brightness sensitivity. Because these data are quite new and still in a preliminary state, we use them here primarily for a qualitative comparison to the MUSE results in Section 3.6.

We trace molecular gas surface density using CO (2–1) maps from the PHANGS–ALMA survey (Leroy et al. 2021). These data have similar resolution to the MUSE H $\alpha$  maps and we use them to assess the presence of cold, molecular gas in the vicinity of H II regions where SNe are detected. CO (2–1) emission is a standard tracer for the cold, dense, star-forming phase of the ISM (for a review see Bolatto et al. 2013). Here we primarily focus on the detection of CO emission, reporting if there is significant (signal-to-noise  $>3$ ) CO (2–1) emission present. For a more detailed analysis of CO (2–1) emission at the sites of SNe explosions in the PHANGS galaxies, with more description of how we handle the PHANGS–ALMA CO (2–1) data, see Mayker Chen et al. (2023).

We also use near-infrared (near-IR) emission to trace the overall distribution of stellar mass in our targets. This allows us to construct control measurements that predict the amount of chance coincidence between SNe and H II regions expected for normal (not just massive) stars. We trace the surface density of stellar mass using near-IR ( $3.6 \mu\text{m}$ ) maps from the Infrared Array Camera (IRAC) on the Spitzer Space Telescope. These were mostly obtained or reprocessed as part of the S<sup>4</sup>G survey Sheth et al. (2010), and details of their processing and origin in the context of PHANGS are described in Querejeta et al. (2021). We use the near-IR intensity for this purpose and do not make any corrections to account for local variations in the stellar mass-to-light ratio.

### 2.2. SN Selection

Following Mayker Chen et al. (2023), we gather a population of recent ( $<125$  yr) SNe using the Open Supernova Catalog (OSC)<sup>21</sup> and the Transient Name Server (TNS).<sup>22</sup> We are interested in SNe that have exploded recently and therefore have not had enough time to influence their surrounding environment. A typical early-stage SN shock with a velocity of  $10^4 \text{ km s}^{-1}$  (Draine 2011) will only have expanded by  $\sim 1$  pc in 100 yr, which is much smaller than the resolution of our data. The OSC also records supernova remnants, which can confuse this selection. To avoid including these, we only select SNe that have a recorded discovery date.

We select a population of 32 SNe within 10 galaxies in the PHANGS–MUSE galaxy footprints. Table A1 lists the SNe along with their host galaxy, type, R.A., and decl., whether they are included in our project sample, and the reference paper used for their type classification. A total of 36 SNe in 11 galaxies were originally identified, but we do not analyze two SNe (SN2013ej in NGC 0628 and SN1979C in NGC 4321)

<sup>21</sup> Accessed on 2022 January 26, but no longer accessible online.

<sup>22</sup> <https://www.wis-tns.org/> (accessed 2023 December 30).

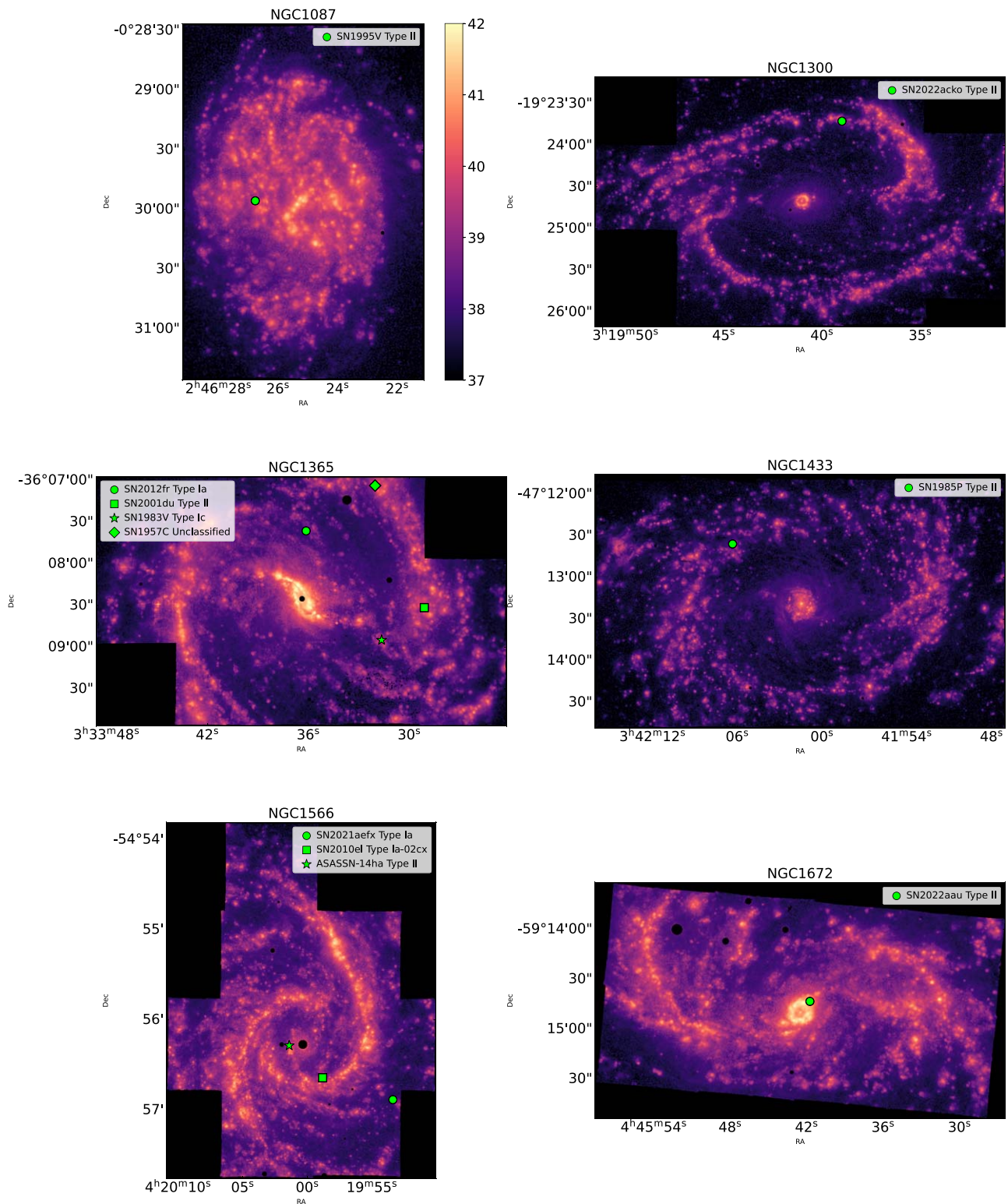


**Figure 1.** Recent SNe (green symbols) that occurred within the footprint of the PHANGS–MUSE survey (Emsellem et al. 2022) plotted over PHANGS–MUSE images of extinction-corrected  $H\alpha$  intensity on the same logarithmic stretch, shown in the color bar. Black dots are where foreground stars have been removed from the image. Each SN in each galaxy is given a unique marker shape, with details of each galaxy given in Table A1 and each SN given in Table A2. The Appendix presents “zoom in” images around each SN and comparison to higher-resolution HST  $H\alpha$  mapping. Continued in Figure 2.

because they lie just outside of the map coverage. We remove SN2019krl in NGC 0628 because of uncertainty in its type classification and the likelihood that it is instead a nonterminal explosion (Andrews et al. 2021), and finally we remove SN2017gax in NGC 1672 because it was imaged shortly after

the explosion and the SN’s light has dominated the spectrum. This reduces our working sample to 32 SNe within 10 galaxies, 19% (6/32) are SNe Ia, 59% 19/32 are SNe II, 13% (4/32) are SESNe, and 9% (3/32) are unclassified. We show their locations in Figure 1. In Table A2 we report the type

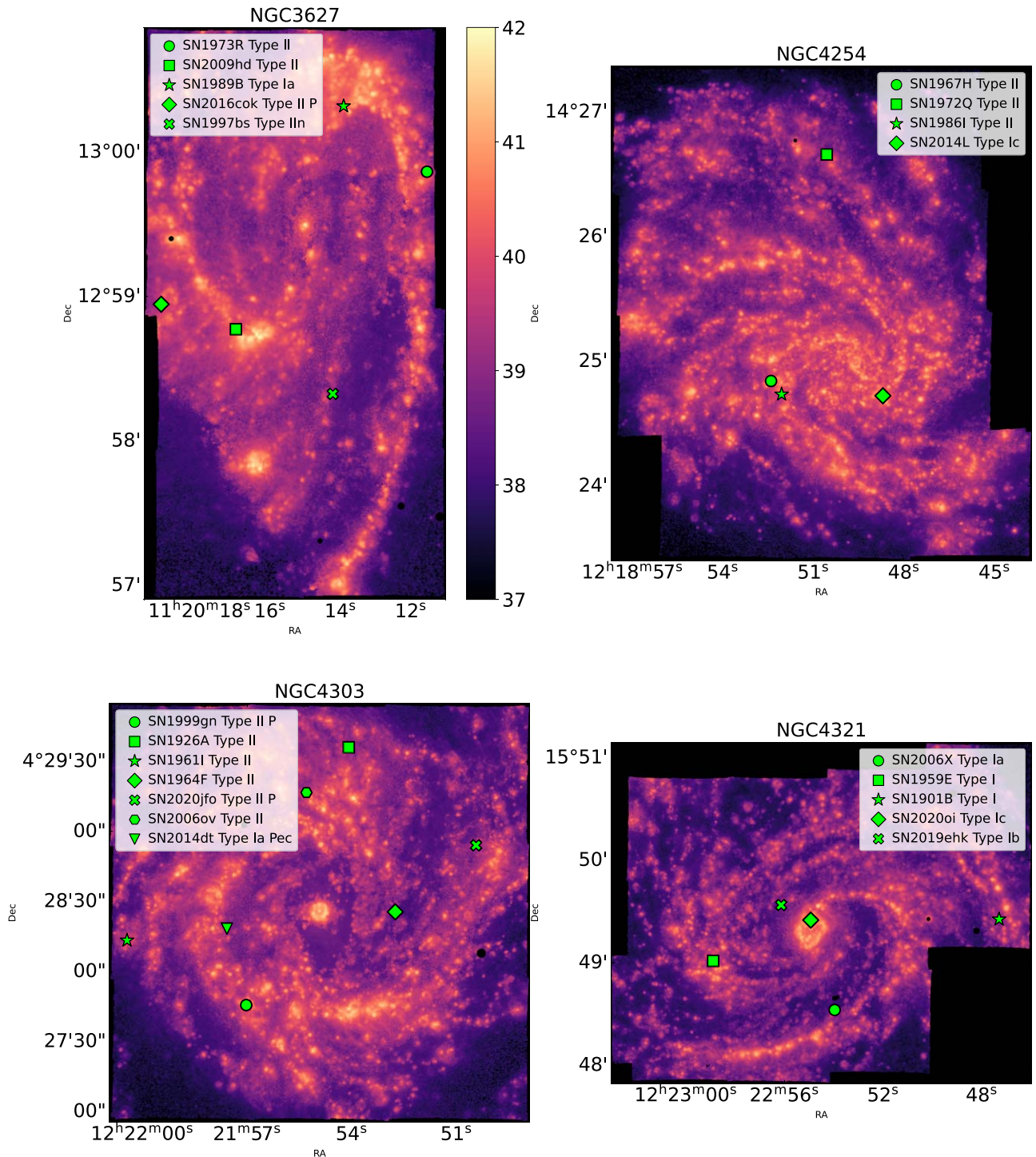


Figure 2. Figure 1 continued.

classification, native H $\alpha$  map resolution, H $\alpha$  intensity measured at the SN site, the velocity dispersion, extinction, H II region status, BPT diagnostic line classifications, presence of CO (2–1) emission, directly measured H II region metallicities (when available) and calculated metallicities using galaxy gradients, galactocentric radius, and effective radius of each SN site.

The measurement of the spatial coincidence of SNe and H $\alpha$  emission is limited by the resolution of the MUSE data and the positional accuracy of the SN location. The MUSE resolution usually represents the limiting factor for SNe detected in the

last few decades, but for the older half of our sample, the location of the SNe may also contribute to uncertainty.

Assessing positional uncertainties in the SNe precisely is complicated because the OSC, TNS, and the vast majority of SN discovery papers do not report positional uncertainties. To estimate a typical positional uncertainty for our SNe, we examine a wide selection of individual SN discovery papers and observe the change in the reporting confidence from discoveries that took place in the mid-1900s and those that have occurred in the last few years. We find that SNe that have occurred in the last  $\sim 20$  yr are more likely to report

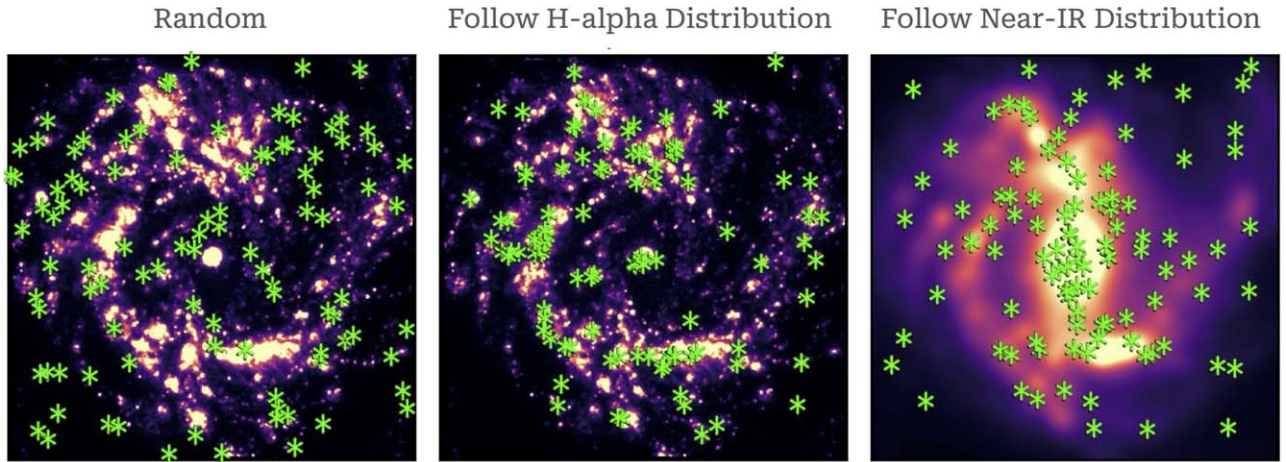


**Figure 3.** Three models for SN placement in galaxies, each illustrated by placing 100 model-generated SNe in NGC 4303. From left to right—Model 1: the SNe are randomly placed across the footprint of the MUSE H $\alpha$  map with equal probability assigned to each pixel. Model 2: the SNe are placed based on a probability distribution that follows the distribution of H $\alpha$  intensities in the MUSE H $\alpha$  map. Model 3: the SNe are placed based on a probability distribution that follows the near-IR light in the Spitzer 3.6  $\mu\text{m}$  map and therefore approximately traces the overall distribution of stellar mass.

uncertainties in their position—ranging from  $0''.1$  to  $1''$  (see, e.g., Evans & McNaught 2003; Monard 2008; Pignata et al. 2009) and recent SN discovery papers that do not report uncertainty, their position is reported to the nearest  $0''.1$ – $1''$  as well. Because of this, we assume that for modern SN searches like ASAS-SN (Shappee et al. 2014; Kochanek et al. 2017), a typical positional uncertainty will be  $\lesssim 1''$ . However positional uncertainties for early SNe, such as SN1926A, could be as high as  $\sim 10''$ .

Half (16/32) of our sample has occurred within the last 20 yr. We consider that for these, the positional uncertainty is of the same order as the angular resolution of MUSE maps, while for the remaining half, the uncertainty in the astrometry is dominated by the uncertainty in the reported SN location.

### 2.3. Relative Positions of SNe, H II Regions, and Statistical Controls

We measure whether each SN occurs inside a known H II region, note the distance to the nearest pixel in the H II region<sup>23</sup> for SNe outside H II regions, and record the intensity of H $\alpha$  emission at each SN. Because our galaxies have extended H $\alpha$  emission and often have a large fraction of their area covered by H II regions, we also construct several control scenarios to assess the probability of random coincidence. Similar to Mayker Chen et al. (2023), we use several model populations as controls to help interpret our measurements for our real SN sample. We consider these cases:

1. *Purely random:* In this case, SNe are equally likely to occur in each pixel of the map, leading to a purely random distribution.
2. *Random within the local region around the SN:* We also consider a scenario where the SN occurs randomly at a position within a  $500 \text{ pc} \times 500 \text{ pc}$  or  $1 \text{ kpc} \times 1 \text{ kpc}$  box centered on the SN explosion. This is intended to capture that some other variable might cause SNe to explode in a general region of the galaxy and to test for chance small-scale coincidence between H II regions and SNe once the general SN location is set.

3. *Following the H $\alpha$  distribution:* In this case, the likelihood for an SN to occur on any pixel is proportional to the intensity of H $\alpha$  emission at that location in the MUSE maps. We expect our population of CCSNe to be better represented than the SNe Ia for this model due to the short delay times of their progenitors.
4. *Following the stellar disk traced by near-IR emission:* In this final control case, SNe are drawn based on the intensity of the near-IR maps described in Section 2. This helps model SNe that trace the distribution of stellar masses, which should be appropriate for populations with longer delay times, e.g., SNe Ia (Maoz et al. 2014; Anderson et al. 2015a; Cronin et al. 2021).

We generate 1000 model SNe for each SN in our sample. This gives us a total of 32,000 model SNe from 10 galaxies generated for each model. We calculate the expected coincidence between these model distributions and the Groves et al. (2023) H II regions. Following Mayker Chen et al. (2023) we also calculate the expected overlap with CO emission and with both CO emission and the presence of an H II region in the line of sight for each case. Figure 3 shows examples of these control distributions for one galaxy. Table 1 reports the coincidence between SNe and H II regions expected for each of these models. We also compare the cumulative distributions of the models to our real SN sample in Figures 6 and 8.

## 3. Results Comparing H $\alpha$ Emission to SN Location

In Figures 1 and 2 we plot the PHANGS–MUSE H $\alpha$  maps for our sample of galaxies with SNe. We show the maps at their native resolution, which ranges from  $0.78$  to  $1''.16$ , and mark the locations of recent SNe in each galaxy. In this section we analyze the fraction of SNe that appear coincident with an H II region (Section 3.1) and compare these results with expectations from SSP models (Section 3.3), measure the distance of SNe from H II regions (Sections 3.4, 3.2), the intensity of H $\alpha$  emission at the sites of SNe (Section 3.5), and the relative position of H $\alpha$  emission and SNe at high resolution (Section 3.6).

<sup>23</sup> The borders of H II regions correspond to HIIphot masks.

**Table 1**  
Occurrence of SN Sample (Top Half), Emission, and Pixel Counts (Bottom Half) in the Line of Sight of ISM

Type	H II Region	H II + CO	CO Only	Excess
All SNe (32)	41% (13)	34% (11)	22% (7)	$7.6\% \pm 8.7\%$ <sup>a</sup>
SESNe: IIb/Ib/Ic (4)	100% (4)	75% (3)	0% (0)	$38\% \pm 23.5\%$ <sup>a</sup>
SNe II (19)	42% (8)	37% (7)	21% (4)	$10.5\% \pm 11.3\%$
SNe Ia (6)	17% (1)	17% (1)	17% (1)	...
Unclassified (3)	0% (0)	0% (0)	67% (2)	...
H $\alpha$ Emission	73%	69%	16%	...
Near-IR (3.6 $\mu$ m) Emission	32%	23%	28%	...
Random Map Pixel	14%	9%	22%	...
Random Local (1 kpc)	32%	26%	34%	...
Random Local (500 pc)	36%	30%	31%	...

**Note.**

<sup>a</sup> The probability of control selecting 4/4 sites in H II regions is 1.2%.

### 3.1. Fraction of SNe in H II Regions

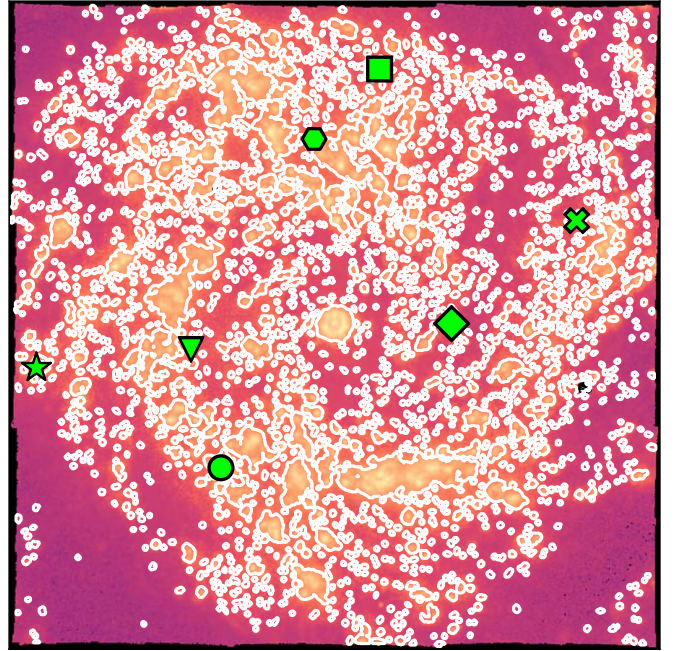
As described in Section 2, we use the Groves et al. (2023) nebular catalog to identify pixels where H II regions lie along the line of sight through the galaxies. Figure 4 illustrates these H II region contours for one target, NGC 4303. It shows that H II regions cover a large area of the disk of the galaxy and encompass much of the bright H $\alpha$  emission. Across our sample, about 74% of the total H $\alpha$  emission arises from pixels identified as H II regions in the native resolution maps. The rest of the emission is associated with the extended diffuse ionized gas component (see, e.g., Belfiore et al. 2022).

Table 1 summarizes our basic results. We find that 41% (13/32) of our SNe occur coincident with an H II region. For comparison, across our galaxy sample, 13.7% of map pixels are coincident with H II regions. This means that if assigned to pixels randomly, 1/7 (4.4/32) of all SNe would occur along a line of sight that intersects an H II region.

The PHANGS–MUSE images often cover a large portion of a galaxy, including both the dense, high surface density inner regions and spiral arms and the more extended, lower surface density regions. As a result, some of the observed coincidences between SNe and H II regions may result from the SNe simply occurring in denser parts of galaxies where both H II regions and stars are more common. To account for this, we also construct a set of more localized comparisons, in which we compare the fraction of SN locations with detected H II regions to only the fraction of area covered by H II regions in nearby pixels. Here we define “nearby” as boxes  $500 \times 500$  pc or  $1 \times 1$  kpc in size centered on each SN. The goal with this more stringent control is to test the idea that SNe occur specifically concentrated within H II regions.

Adopting this more stringent control, the results indicate that 32% of pixels within  $1 \text{ kpc} \times 1 \text{ kpc}$  local regions centered on our SN sites belong to a Groves et al. (2023) H II region. This fraction increases to 36% if we instead consider fields of size  $500 \text{ pc} \times 500 \text{ pc}$ . This means that if we allow SNe to occur in a given part of the galaxy, then we expect that  $\sim 32\%$ – $36\%$  will

## NGC4303



**Figure 4.** H II regions and recent SNe in NGC4303. As Figure 2 for NGC 4303 but now the white contours show the extent of the nebular region catalogs from Groves et al. (2023) and Santoro et al. (2022).

occur along the line of sight to an H II region simply due to random chance.

As an alternative control, we also examine the fraction of total near-IR emission arising from within the H II regions. The near-IR traces the overall distribution of stellar mass. We find that 32% of near-IR emission emerges from regions coincident with H II regions. Similar to the “local region” control, treating the near-IR as a control distribution suggests that we would expect a third of our SN sample, or about 10 SNe, to lie within the H II regions just by coincidence alone.

Thus both the local region control or using the near-IR suggest that we might expect one-third of SNe to occur near an H II region by chance. We emphasize that this calculation is focused on coincidence *along the line of sight at the MUSE resolution*. The actual position of the SNe along the line of sight is uncertain and the MUSE sizes may represent overestimates of the true H II region sizes (e.g., Barnes et al. 2022, and see below). On the other hand, it is still of physical interest that so many SNe appear to be located *near* (rather than in) H II regions by coincidence. This proximity provides an opportunity for interactions between SNe and ionized gas interactions during the SN remnant phase. SN explosions in or near H II regions, even if by coincidence, also represent locations where different modes of feedback potentially amplify one another, indicating places where multiple generations of SNe are able to clear out larger volumes of gas.

Our measured SNe–H II region coincidence of  $\approx 41\%$  is higher than either the  $\approx 32\%$ – $36\%$  suggested by the local models or the  $\approx 32\%$  suggested by the starlight distribution. This indicates that some SNe *do* preferentially occur in H II regions, but also that controlling for random coincidence is critical to estimate the rate. Using a binomial distribution we estimate the uncertainty due to stochasticity to be  $\pm 8.7\%$ .

Contrasting these local covering fractions with the fraction of SNe coincident with H II regions, we find a general excess of

$7.6\% \pm 8.7\%$  of all SNe to be associated with H II regions. In the next section, we separate our SN sample by type, specifically focusing on CCSNe which we expect to be more associated with star-forming regions of galaxies.

### 3.2. Breakdown by Type

Table 1 shows the fraction of SNe coincident with H II regions broken down by type. We find that 20% (1/6) of SNe Ia, 42% (8/19) of SNe II, and 100% (4/4) of our stripped-envelope SNe (SESNe; Types II, Ib, and Ic) occur coincident to H II regions. The sense of these results is consistent with that found by previous lower-resolution work (e.g., Anderson et al. 2012, 2015b; Anderson 2014; Audcent-Ross et al. 2020), which identified that increasing progenitor mass leads to increasing association with bright H $\alpha$  emission. As a reminder, the progenitor mass sequence from lowest to highest is believed to be SNe Ia  $\rightarrow$  SNe II  $\rightarrow$  SESNe.

The mild 6% excess of SN in H II regions becomes more prominent when we consider only CCSNe. CCSNe (II and SESNe) have an excess of  $19.2\% \pm 10.4\%$  coincident with an H II region, and when considering only SESNe we find an excess of  $38\% \pm 23.5\%$ . Although the SESNe sample is extremely small (only four SNe) the probability of our controls randomly placing SNe coincident to an H II region 4/4 times is only 1.2%. The physical association is also expected because SESNe are thought to originate from the most massive stars. These will also be the earliest stars to explode. They may therefore be within or near their birth sites, and likely to still be bright in H $\alpha$  emission.

Thus, with the caveat that our controls suggest that random overlap may explain some of our measured associations, the differences among types match physical expectations. Because H II regions mark where young, massive stars have formed very recently, the SNe with the highest mass progenitors should be more likely to occur near these regions as they explode first. H II regions have lifetimes of  $\lesssim 5\text{--}10$  Myr, similar to the lifetime of a single massive star. Lower-mass CCSNe with delay times of  $\sim 10\text{--}30$  Myr are more likely to outlive their birth H II region and will have more time to migrate away from the high-density regions where they formed. We do not expect SNe Ias to have an association with star-forming regions due to their long delay times, but we do expect that a fraction of SNe Ias will occur coincident with an H II region just because the H II regions cover an appreciable fraction of the galaxy.

We note that none of the unclassified SNe occur in H II regions. By contrast, Mayker Chen et al. (2023) found that most of the unclassified SNe occurred in regions that did have bright CO emission, but they worked with a sample about twice as large as the current work.

Finally, we note that our limited sample size might lead to a sample that does not accurately reflect the broad SN landscape. Of specific interest here, previous SN surveys find that SESNe make up 25%–30% of CCSNe (Smartt 2009; Li et al. 2011), while only 12.5% of our sample are SESNe. Given the high degree of association that we observe between the SESNe and the H II regions here, a more representative sample with more SESNe would likely show a somewhat higher overall coincidence between SNe and H II regions.

### 3.3. Comparisons to Expectations from SSP Models

Our analysis suggests that  $\sim 20\%$  of CCSNe preferentially explode in H II regions. How does this compare to expectations? In Figure 5 we plot results for an SSP using the default assumptions from STARBURST99 (SB99 Leitherer et al. 1999, 2014). We plot the cumulative distribution functions (CDFs) as a function of time for both the number of SNe explosions and H-ionizing photon production, which should map to H $\alpha$  emission.

In the SB99 model, the delay time for CCSNe ranges from 3 to 37 Myr, with the first 20% of SNe occurring by 7.11 Myr. This is consistent with the H $\alpha$  brightness drop off which occurs significantly by  $\approx 7$  Myr and the CDF of H $\alpha$  emission (or H-ionizing photon production) shows that most of the H $\alpha$  has been produced before that time.

If star-forming regions in our targets are indeed accurately described by an ensemble of SSPs, then our inferred SNe associated with H $\alpha$  would likely need to be associated with high-mass progenitor stars with lifetimes shorter than  $\approx 7$  Myr or with a binary core-collapse SN production channel that operates on a similar timescale. To be precise, the first 20% of the SNe in this SSP calculation occur by 7.11 Myr and represent stars with masses  $> 24.9 M_{\odot}$ .

In reality, the picture will be more complex than this. Supernova explodability work by Sukhbold et al. (2016) shows that the most massive stars have a much lower frequency of exploding, although there is no clear-cut boundary between explosions and nonexplosions, the probability of successful explosions is less as you go above  $20 M_{\odot}$ , with the most massive stars requiring significant mass loss in order to explode. On the other hand, binary star systems extend the H $\alpha$ -emitting lifetime and open more complex mappings between progenitor mass and explodability and different evolutionary timescales (e.g., Eldridge 2011; Vartanyan et al. 2021; Nguyen et al. 2022; Patton et al. 2022). Likely, many of the regions we examine are also not SSPs but host multigeneration or extended-duration star formation (Rahner et al. 2017). Another caveat is that the Starburst99 models assume a fully sampled initial mass function, which is likely valid for the galaxy as a whole but may not be true for many of the individual regions, depending on the mass of the powering star cluster.

### 3.4. Distance from SNe to H II Regions

Even when SNe are not directly associated with H II regions, we might expect those associated with very massive stars to be near such regions. To test this, we also calculate the distances to the nearest pixel tagged as an H II region in the Groves et al. (2023) catalog for each of our SNe.

The left panel of Figure 6 shows the kernel density estimation (KDE) of the distances from each SN to the nearest H II region, where the SN population is separated by type. Vertical color-and-style-coded lines mark the median distance value for each SN type. We shade the typical MUSE spaxel size in gray. The figure shows that our SESNe are always occurring coincident to H II regions, our SNe II are more frequently found away from H II regions than our SESNe, with a median distance of 10 pc. Although our SNe Ia are often found farther away from H II regions with a median distance of 110 pc, they are still relatively close. The overall low distances even for SNe not directly associated with H II regions reflect that PHANGS–MUSE targets the actively star-forming parts of



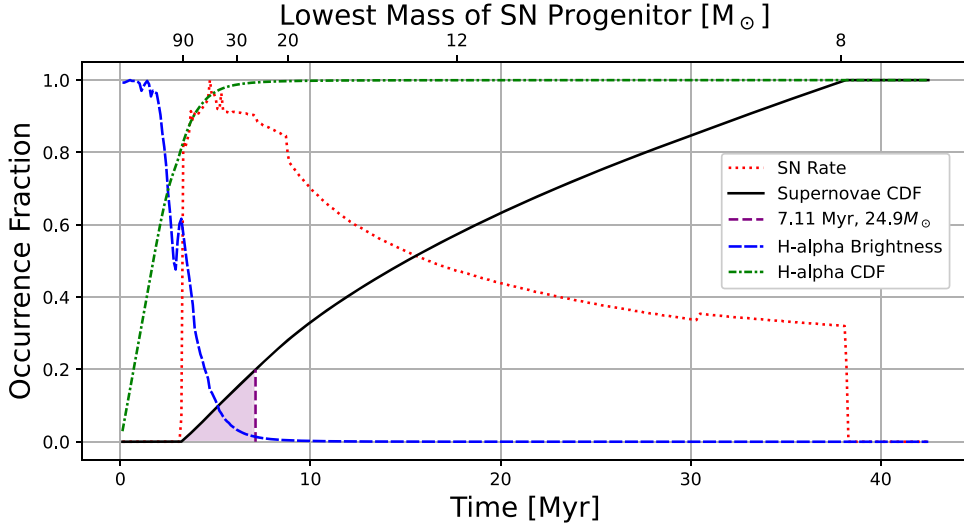


**Figure 5.** CDF of SNe over time from a simple stellar population modeled with STARBURST99. The CDF of the SNe is plotted with a solid black line, the normalized SN rate is plotted with a dotted red line, the CDF of  $H\alpha$  emission is plotted with a dotted-dashed green line, and the normalized  $H\alpha$  brightness with a dashed blue line. In purple, we shade the SN CDF to indicate when it reaches the level of excess CCSNe (20%) that we find coincident with H II regions. We also mark the delay time (7.11 Myr,  $24.9M_{\odot}$ ) that accounts for that excess with a dashed purple vertical line.

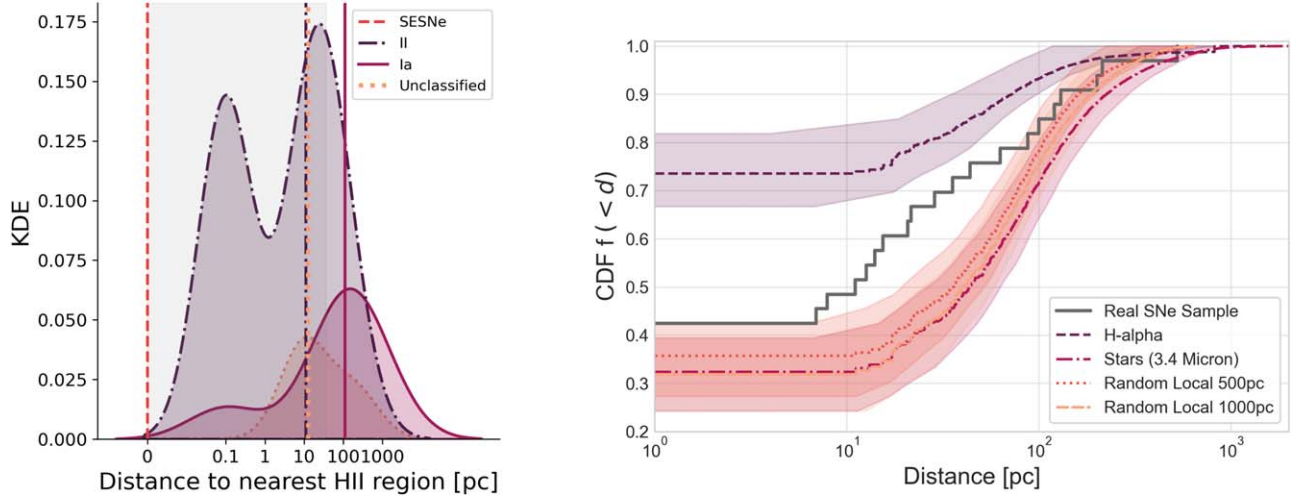


**Figure 6.** Distances to nearest H II region. Left: KDE of the distances from each SN site to the nearest H II region. SNe with distances less than 1 pc are found within an H II region. SNe II are represented with dashed-dotted, dark-purple; SNe Ia with solid red-purple; SESNe with dashed magenta; and unclassified SNe with dotted peach. Vertical color-and-style-coded lines mark the median distance value for each SN type. Gray shaded region marks the pixel scale. Right: CDFs of the distances to the nearest H II region for our real SN sample and three modeled populations. Our real SNe sample is drawn with a dark-gray line. The randomly generated SNe sample is drawn from the local (500 and 1000 pc) map around each SN site. The 500 pc random pull sample is plotted with a dotted magenta line and the 1000 pc with a dashed peach line. The population generated from the  $H\alpha$  distribution is plotted as a dashed, dark-purple line, and the stellar disk distribution as a dashed-dotted red-purple line. The transparent shading represents the 16th–84th percentile values from 1000 random pulls each the size of our observed SN sample from each model distribution. We find that our SESNe are overwhelmingly located in the line of sight to our H II regions, while our SNe Ia sample tends to be less associated with H II regions, and our SNe II are somewhere in between. Our real SN sample is distributed between our  $H\alpha$  model sample and our stellar disk and random local models.

galaxies. As a result,  $H\alpha$  emission is prevalent throughout the maps and even an SN associated with an older progenitor is still likely to occur close to an H II region.

Similar to Mayker Chen et al. (2023), we compare the measured SNe–H II region separations for our real SN sample to those produced for the model populations described in Section 2.3. In the right panel of Figure 6, we show the cumulative distributions of the distances to the nearest H II region for both our real SN sample (32 SNe) and each of our four model SN populations (32,000 SNe generated for each model). We find that the distribution of our real SN population lies between the model population that follows the distribution of  $H\alpha$  emission and the model populations drawn from either

the distribution of stellar mass or local regions around the real SN location. This reinforces the results above that while SNe are more associated with H II regions than the general stellar population, they do not directly trace the distribution of  $H\alpha$  emission.

### 3.5. Intensity of $H\alpha$ Emission at the Locations of Recent SNe

So far, we have considered only whether a sight line is coincident with an H II region. The intensity of  $H\alpha$  emission provides additional information, tracking the production rate of ionizing photons and potentially conveying additional information on the distribution of massive, young stars within an

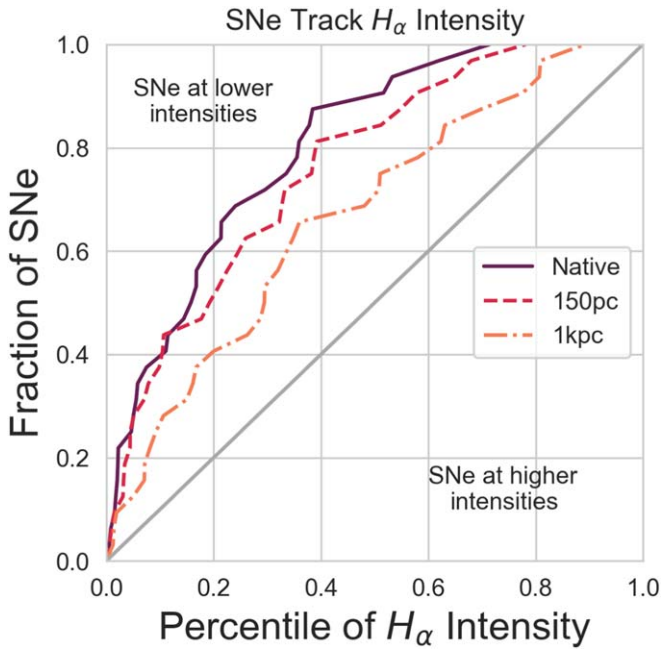


**Figure 7.** Normalized cumulative rank (NCR) plot of the association of SNe with  $H\alpha$  emission at native, 150 pc, and 1 kpc resolutions. Results for the PHANGS–MUSE native resolution (44–109 pc) are plotted with a solid purple line, 150 pc resolution results are plotted with a dashed magenta line, and 1 kpc resolution results are plotted with a dashed–dotted salmon line.

individual H II region. To leverage this information, we also measure the intensity of  $H\alpha$  emission at the site of each of our SNe and report the results in Table A2.

Figure 7 shows the normalized cumulative rank (NCR) of SNe relative to the distribution of  $H\alpha$  emission at native, 150 pc, and 1 kpc resolutions. An excellent overview of the NCR method is given in James & Anderson (2006). Briefly, we sort the pixels in each  $H\alpha$  map by  $H\alpha$  intensity, assigning a percentile in the CDF to each. Then we note the percentile of the  $H\alpha$  intensity CDF for the pixel at which each SN occurs and so construct the NCR of SNe relative to  $H\alpha$ . If the SNe occur in locations that track the distribution of  $H\alpha$  intensity, then the measured curve will follow a line with slope unity. This analysis emphasizes the coincidence between SN sites and H II regions and could be impacted if the SNe and stellar winds cleared the surroundings of ionized gas. Although we do not expect our SN sample to have had time to dramatically influence their local environments, we address this in Section 3.6 where we plot the local ( $500 \times 500$  pc) environments of each SN and look for signs of shell-like morphology in the  $H\alpha$  emission.

Consistent with the finding above that SNe appear in  $H\alpha$ -rich parts of galaxies, but not necessarily within H II regions themselves, Figure 7 shows that our SNe sample tracks the  $H\alpha$  emission more directly as the resolution becomes coarser. The fact that the lines are above and to the left of the one-to-one line means that actual SNe occur at lower  $I_{H\alpha}$  on average than we would expect if the probability of finding an SN tracked the distribution of  $H\alpha$  emission exactly. The better agreement at coarser resolution reflects that at lower resolution, the beam of the telescope captures more of a region-average measurement of star formation activity, while at higher resolution we are able to better isolate individual H II regions, and we observe that SNe appear somewhat offset from these regions.

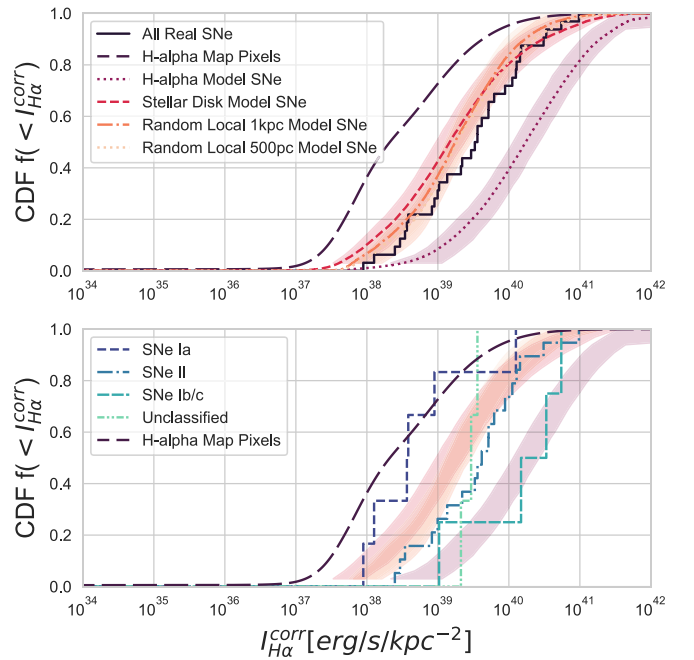


**Figure 8.** CDFs of the extinction-corrected  $H\alpha$  emission intensity distributions for our real SN sample, for all the map pixels, and for our populations of model SNe. In the top panel, we compare the models to our whole real SN sample. In the bottom panel, we maintain the same comparison, but instead sort our SNe by type. The whole real SN sample (32 SNe) is drawn with a solid black line, the map pixels are drawn with a long-dashed, dark-purple line. The  $H\alpha$  model SNe are drawn with a dotted purple line, the stellar disk model SNe with a dashed pink line, and the random local models are drawn with orange dotted–dashed and yellow dotted for 1 kpc and 500 pc local boxes respectively. Behind each model line, we use transparent shading to represent the 16th–84th percentile values from 1000 random pulls, each the size of our observed SN sample, from each model distribution. The shaded percentiles are drawn on the lower plot as well but we remove the lines for readability. In the lower plot we sort our real SN by type, plotting the SNe Ia with a dashed dark blue line, the SNe II with a dotted–dashed blue line, the SESNe (SNe Ib/c) with a closely dashed teal line, and the unclassified SNe with a dotted–dotted–dashed light green line. Note the increasing association with higher intensity  $H\alpha$  emission as progenitor mass increases.

In Figure 8 we plot the CDF of  $H\alpha$  intensities at the sites of our real SN sample (32 SNe), the CDF for all  $H\alpha$  emissions at the native (44–109 pc) resolution of the MUSE maps, and the CDF of  $H\alpha$  intensity generated for each of the three model populations described in Section 2. In the top panel, we show results for our whole SN sample, and in the bottom panel, we separate the SNe by type. The shaded regions represent the 16th–84th percentile range covered by repeat realization of the models.

Similar to results with the distances from H II regions, we find that the distribution of  $H\alpha$  intensities at the real SN sites falls somewhere between the distributions for the model SNe generated from the near-IR light and the model SNe generated from the  $H\alpha$  intensity. We expect that the higher mass progenitors would have a closer association with the  $H\alpha$  distribution, while the lower-mass CCSNe and SNe Ia would have a distribution that more closely resembles that taken from the overall stellar population traced by near-IR emission.

When we separate the SNe by type, we find the SNe Ia to exhibit a similar distribution to the map pixels or the near-IR emission. This agrees well with the expected lower-mass range and wide age range of SN Ia progenitors. As the progenitor mass increases, we find an increasing association with higher  $H\alpha$  intensity values, reaffirming the results of previous works

## SN1995V (NGC1087) Type II

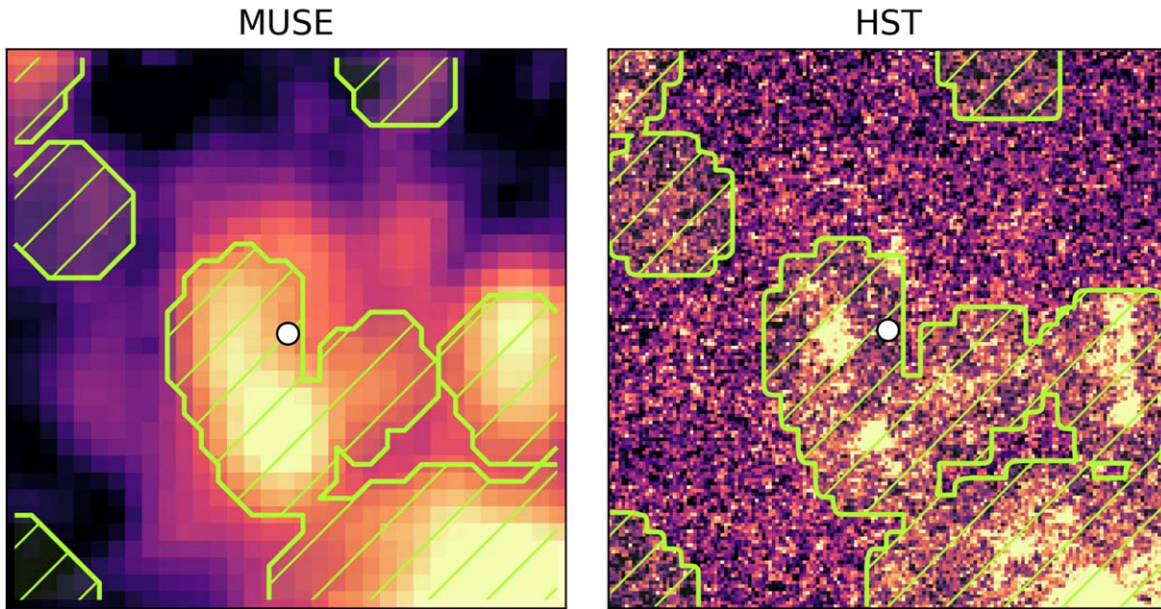


**Figure 9.** Example  $500 \text{ pc} \times 500 \text{ pc}$  zoom in for SN1995V (Type II) in NGC 1087. The left panel shows  $\text{H}\alpha$  intensity from the PHANGS–MUSE maps. The right panel shows  $\text{H}\alpha$  emission from the same region at a higher than  $\approx 0''.1$  resolution from new narrowband HST mapping (Chandar, A. Barnes et al. 2024, in preparation) In both panels, the hatched green regions indicate the footprint of the Groves et al. (2023) nebular region catalog.

(e.g., Anderson et al. 2012, 2015b; Anderson 2014). Of particular note, the SESNe (SNe Ib/c) show a distribution very similar to the  $\text{H}\alpha$  maps themselves, supporting a direct association with high-mass progenitors.

### 3.6. Zooming in on Individual Regions and Comparison to Hubble Space Telescope Imaging

In Figures A1–A3 in the Appendix, we zoom in to each SN site, plotting  $500 \text{ pc} \times 500 \text{ pc}$  cutouts of  $\text{H}\alpha$  emission around each of the 32 SNe in our sample as well as marking the footprint of regions in the Groves et al. (2023) nebular catalog. We show an example of one such cutout in the left panel of Figure 9. These cutouts demonstrate that many of these SNe appear in or near regions rich in  $\text{H}\alpha$  emission. They also show that, while many SNe occur within the footprint of the nebular regions, none are actually coincident with the local peak of  $\text{H}\alpha$  emission. Instead, the SNe tend to lie off to the side, often near the edges of the regions and are associated with lower intensity  $\text{H}\alpha$  emission.

To test this hypothesis further, we take advantage of very new, high-resolution ( $\sim 0''.1$ ) narrowband  $\text{H}\alpha$  imaging of these targets using the Hubble Space Telescope (P.I. R. Chandar; Chandar, A. Barnes et al. 2024, in preparation). As illustrated in the right panel of Figure 9, these data have been processed following a scheme similar to that described in Lee et al. (2022) and Barnes et al. (2022). Here we use the data to provide a  $\sim 10\times$  sharper view of the H II regions compared to MUSE. Though the surface brightness sensitivity of HST does not match MUSE, the resolution of these data ( $\sim 5\text{--}15 \text{ pc}$ ) more closely matches the physical sizes of H II regions seen in the Milky Way (e.g., Anderson 2014).

In Figures A4–A9 we remake the cutouts above using these HST  $\text{H}\alpha$  data, again marking the locations of the Groves et al. (2023) H II regions and significant CO(2–1) emission. At the diffraction-limited, high resolution of HST, the H II regions

seen by MUSE are significantly more resolved, appearing smaller and significantly better defined. Many SNe located within the edges of H II regions in the MUSE maps (e.g., SN1995V and SN1983V) appear offset from the H II regions in the sharper HST maps. In fact, *none* of the SNe with HST  $\text{H}\alpha$  coverage actually lie on a high-resolution  $\text{H}\alpha$  peak, though we caution that the astrometric precision with which the SNe are located makes it hard to draw a firm conclusion.

Examining these images, especially the HST images, reinforces the statistical finding above that a large fraction of the SNe coincident with the Groves et al. (2023) H II regions are likely to represent chance alignments. The overall active star-forming nature of the regions where the SNe occur and the relatively coarse physical resolution of the MUSE data lead to a large fraction of chance overlaps.

We might expect that pre-SN feedback would result in a shell-like morphology for the  $\text{H}\alpha$ , with lower densities of ionized gas surrounding the stellar population and near the site of the SN itself. However, such a morphology is not immediately clear from our images. We overwhelmingly see that our SN sites are off to the sides of the H II region, rather than enclosed at least partially by shells. It is possible that the shells are too small to show up at the MUSE resolution and the lower sensitivity of the HST data.

We caution that the positional uncertainty for the SNe represents a major limiting factor when compared to the HST  $\text{H}\alpha$  data. As Figure A4 shows, even in nearby galaxies, the angular size of individual H II regions and nebulae is very small, so placing the SNe precisely relative to these features requires astrometric precision of order  $0''.1$ . Given this, future work that leverages HST and JWST to constrain the origin and impact of SNe will require high-quality astrometric positions. With this in mind, we are reassured that many of the SNe that show this characteristic near-but-not-in appearance have been recently discovered and have correspondingly secure astrometry. Our results suggest that SN

feedback is not occurring at the centers of star formation sites, and could have implications for clustered feedback simulations.

Finally, we note that in our previous work Mayker Chen et al. (2023), we found a similar result when comparing the SN sites to molecular gas emission. The SNe associated with CO emission often appeared displaced from the CO peaks and near the edges of the detected regions. Those ALMA CO data have a resolution of  $\approx 1''$ , similar to the MUSE data. It will be telling to see whether at higher resolution the relative location of the SNe and the CO-traced molecular clouds similarly separate.

#### 4. Results Comparing to Other Properties at the SN Location

In Section 3 we examined the coincidence of  $H\alpha$  emission and recent SNe. We found a large fraction of SNe to occur along lines of sight that overlap H II regions but also showed that much of this overlap is likely to be coincidental. Both higher-resolution imaging and statistical analysis suggest that many SNe occur near but not necessarily within H II regions, with our best estimate that there is a  $\approx 20\%$  excess of CCSNe associated with H II regions relative to the controls.

In this section, we expand our analysis to consider other properties near the SN sites, examining the coincidence of  $H\alpha$  and CO emission at SN sites (Section 4.1), the extinction of the ionized gas near SN sites (Section 4.2), and a variety of other diagnostics available from the Groves et al. (2023) and Emsellem et al. (2022) analysis of the MUSE data (Section 4.3).

##### 4.1. $H\alpha$ and CO

Newly formed stars can remain embedded within their parent molecular clouds, with the mass of molecular material commonly traced by CO emission. In recent models of molecular cloud evolution, star-forming regions go through early phases in which newly formed stars still lie within their parent molecular cloud with  $H\alpha$  emission almost undetectable (e.g., Lockman 1989; Kim et al. 2021). Over time, the cloud is exposed to various forms of feedback, which begin to disperse the natal cloud. This dispersal leads to phases in which the cloud is partially dispersed and  $H\alpha$  and CO might be detected together and then as the cold gas becomes mostly dispersed, CO emission vanishes, but the  $H\alpha$  emission remains fully visible (e.g., Kawamura et al. 2009; Kruijssen 2014; Kruijssen et al. 2018; Kim et al. 2022).

By combining the MUSE  $H\alpha$  maps with CO (2–1) measurements from PHANGS–ALMA (see Section 2), we identify which SNe in our sample occur coincident with only CO (2–1) emission, an H II region, both, or neither. To do so, we repeat our control scenarios listed in Section 2.3 and list our results in Table 1. We also overplot the locations of CO (2–1) emission with a signal of 3 times the noise or higher in the zoom panels in the Appendix. Throughout, to count as a detection of CO (2–1) emission, we require a signal-to-noise ratio of 3 in the integrated intensity maps masked with a “broad” mask.<sup>24</sup> Note that here we focus on the joint detection statistics for CO and H II regions in this MUSE sample; Mayker Chen et al. (2023) show a more extensive analysis considering only CO for the full PHANGS–ALMA sample.

We find that 34% of all SN sites are coincident with both an H II region and CO (2–1) emission, while 22% are not associated with an H II region yet are coincident with significant CO (2–1) emission. Contrasting these with the control calculations, the CO-only sightlines appear largely consistent with random coincidence; that is, the percentage of real CO-only sightlines resembles that in the local or near-IR controls. Both the overall H II region and the H II+CO detection rates show an excess relative to these controls.

Similar to the H II regions without CO (2–1) emission, there is an increasing association of progenitor mass with H II + CO (2–1), with 17% SNe Ia, 37% SNe II, and 75% SESNe found in H II + CO (2–1). However, this association breaks down when we consider only CO (2–1) emission without a corresponding H II region, which occurs for 17% of SNe Ia, 21% of SNe II, and 0% of SESNe. Of note, 67% of our unclassified SNe are found in CO-only regions, while none appear associated with H II regions. This follows Mayker Chen et al. (2023) where the unclassified sample had a high correlation with dense CO (2–1) gas. It is possible that these unclassified SNe are exclusively going off in embedded star-forming regions, and the occurrence in high-extinction areas might account for the difficulty in providing classification for the SN, but it is worth noting that the discovery years for our three unclassified SNe range from 1901 to 1959 when both spectroscopic and localization data were more uncertain than for modern SNe.

Our calculations thus show that when an SN appears coincident with an H II region *it almost always also appears coincident with CO (2–1) emission*. Note that previous work on the CO– $H\alpha$  correlation has shown a significant de-correlation between these two tracers at high resolution (see, e.g., Schrubba et al. 2010; Kruijssen et al. 2019; Schinnerer et al. 2019; Pan et al. 2022; Leroy et al. 2023). Those observations helped to establish the picture described above and suggest an important role for pre-SN feedback in clearing gas (e.g., Chevance et al. 2020, 2022). The prevalence of CO detections coincident with SNe and H II regions in our results may seem to contradict this result. However, we note a few points. First, 59% of our SNe are *not* detected coincident with H II regions and there does not appear to be any statistically significant excess of SNe associated with CO outside H II regions. So in good agreement with Mayker Chen et al. (2023), many SNe do appear unassociated with recent star formation or molecular gas. Second, our control calculation suggests that to some degree the correlation that we do see simply reflects that we are capturing SNe in parts of galaxies with higher star formation rates. Finally, we note that the resolution used for this calculation is still coarse. As we saw in Section 3.6, H II regions are still small compared to the MUSE resolution, and the same is likely true of the molecular gas and ALMA. As a result, many of the joint H II region-CO detections likely reflect complex regions with multigenerational star formation blended together by the  $\sim 50$ –150 pc resolution of the VLT and ALMA. Even with these caveats, the result here seems intriguing to us and worth investigating using higher-resolution CO as well as  $H\alpha$  data.

##### 4.2. $H\alpha$ and the Balmer Decrement

The PHANGS–MUSE maps capture the extinction toward the ionized gas along each line of sight via the  $H\beta/H\alpha$  ratio, the Balmer decrement. This allows us to assess the degree to

<sup>24</sup> We are only considering CO (2–1) detections in this work and not accounting for  $\alpha_{\text{CO}}$  variations. See Mayker Chen et al. (2023) for a more detailed discussion of CO (2–1) and SNe.

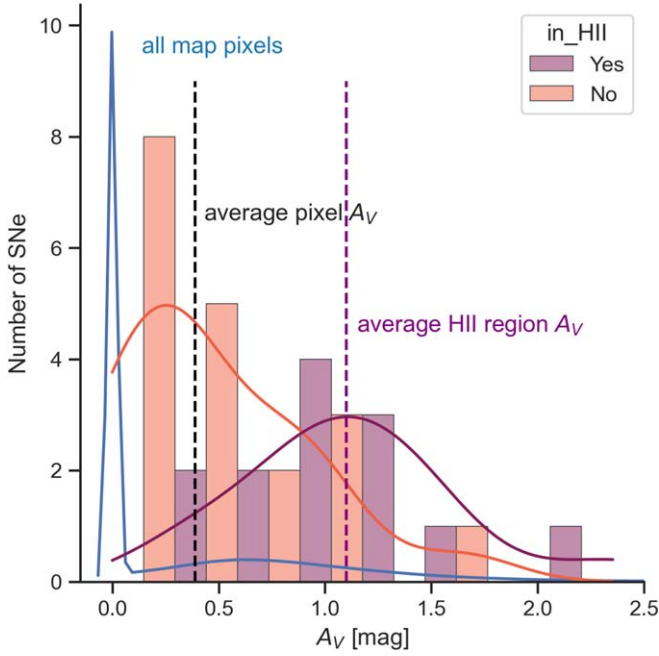


**Figure 10.**  $A_V$  values estimated by Belfiore et al. (2022, 2023) based on the Balmer decrement at each SN site. Lavender bars mark the distribution of  $A_V$  for SNe that are coincident with H II regions. Salmon bars show extinction for SNe not coincident with the H II region and are shifted to the right by one bar width. The KDE of the H II and non-H II populations are drawn in lavender and salmon lines respectively. The KDE for all pixels across all galaxies in our sample is shown by a blue line and the mean for all pixels and all H II regions (with or without SNe) are shown by vertical dashed lines. The average extinction value for all pixels in all maps is  $A_V \approx 0.4$  mag, while the average value for all pixels associated with H II regions is  $A_V \approx 1.1$  mag.

which SNe preferentially occur in high-extinction regions. This local extinction may impact the observability of SNe in surveys of more distant systems. Because gas and dust are mixed, the extinction also gives an alternative probe of the degree to which SNe explode near high-column-density gas. To test this, we measure extinction, expressed as  $A_V$  values, based on the Balmer decrement along the line of sight toward each of our SNe. We adopt the calculations from Belfiore et al. (2022, 2023), who adopt  $R_V = 3.1$  and an O’Donnell (1994) extinction curve. Note that this measurement captures the extinction toward the ionized gas along the line of sight (assuming a foreground screen geometry), which may or may not be identical to the extinction toward the SN itself.

In Figure 10, we plot the resulting histograms of extinction, expressed as  $A_V$ , toward SN sites, separating those coincident with an H II region from those outside H II regions. For comparison, we also plot the KDE of all pixels in the MUSE maps for our targets. The figure shows that our SNe occur in regions with extinction values ranging from  $A_V = 0$ –2.35 mag. The sites that are not coincident with H II regions tend to have lower extinction, median  $A_V = 0.33$  mag with a 16%–84% range of 0–0.92 mag,<sup>25</sup> than the SN sites associated with H II regions, which have median  $A_V = 1.03$  mag with a 16%–84% range of 0.75–1.47 mag. These values resemble typical values found in the MUSE maps overall. In those maps, the mean  $A_V$  outside H II regions is  $A_V \approx 0.4$  mag and the mean  $A_V$  associated with nebular regions is  $A_V \approx 1.1$  mag. The lower

<sup>25</sup> In the Belfiore et al. (2022, 2023) maps, regions without detected H $\beta$  are set to  $A_V = 0$  mag. The diffuse gas has lower overall intensity than H II regions so some of these very low  $A_V$  may be biased low due to the faintness of the lines.

extinction for non-H II regions is well-known (e.g., Equation (9) of Calzetti 2001).

These results indicate that SNe appear associated with typical extinctions, providing no strong evidence that there is a large population of deeply embedded SNe. We note that, because we study very nearby galaxies (compared to the distance out to which SNe tend to be detected in modern broader SN searches), it would be reasonable to expect even quite embedded SNe to be detected in these targets. Despite this, the highest extinction value associated with any SN in our sample is  $A_V = 2.35$  mag.

The fact that we do not appear to find evidence for high extinction toward SNe in normal star-forming galaxies agrees with previous works that show the extinctions around SNe II to be generally small (e.g., Pejcha & Prieto 2015). We note that the evidence for significant populations of hidden or high-extinction SNe comes primarily from studying U/LIRG or starburst systems (e.g., Fox et al. 2021). In those systems, star-forming regions themselves are also found to be associated with high extinction and are primarily visible in the radio or infrared (e.g., Sanders & Mirabel 1996). Thus a more general phrasing of our results might be: our measurements support the idea that SNe occur at typical extinctions for their host galaxies, and are not particularly concentrated toward the highest or lowest  $A_V$ .

The modest extinctions that we measure toward SNe also support the idea of significant pre-SN clearing of material. The typical extinction of  $A_V \sim 1$  mag that we find toward H II regions with SNe corresponds to  $\sim 20 M_\odot \text{pc}^{-2}$  for a typical dust-to-gas ratio. For comparison, the surface densities associated with star formation tend to be  $\sim 100 M_\odot \text{pc}^{-2}$  (e.g., Kennicutt & Evans 2012). Thus, also judging by extinction, most of the SNe in our sample appear to occur in regions where the progenitor has separated from its natal cloud.

### 4.3. Additional Diagnostics

The Groves et al. (2023) catalog provides a treasure trove of information that can be used to further characterize the properties of ionized gas. We note several of these additional diagnostics for each of our SN sites in Table A2:

1. *BPT classifications* ( $[N\text{II}]$ ,  $[S\text{II}]$ ,  $[O\text{I}]$ ): The BPT emission line diagnostics (Baldwin et al. 1981) are used to classify emission as coming from either star-forming regions, active galactic nuclei, low-ionization nuclear-emission-line regions, or a composite of more than one (for more information see Section 4.2 in Groves et al. 2023). We record the BPT emission line diagnostics for each of our SNe that occur along the line of sight to a nebular region. Of the 13 SNe associated with cataloged nebulae, all but two have all BPT diagnostics consistent with arising from star-forming regions (i.e., reported as values of 0.0 in Groves et al. 2023). SN1997bs and SN2019ehk have two out of three emission line diagnostics consistent with star formation with the remaining line diagnostic indicative of an S/N ratio lower than 5 (noninformative, labeled as  $-1.0$ ). This indicates that these are likely H II regions but also might have an additional source of emission within the nebula.
2. *Metallicity* ( $12 + \log(O/H)$ ): In Figure 11 we plot the estimated metallicity at each SN site. These estimates use the metallicity reported in Groves et al. (2023) based on

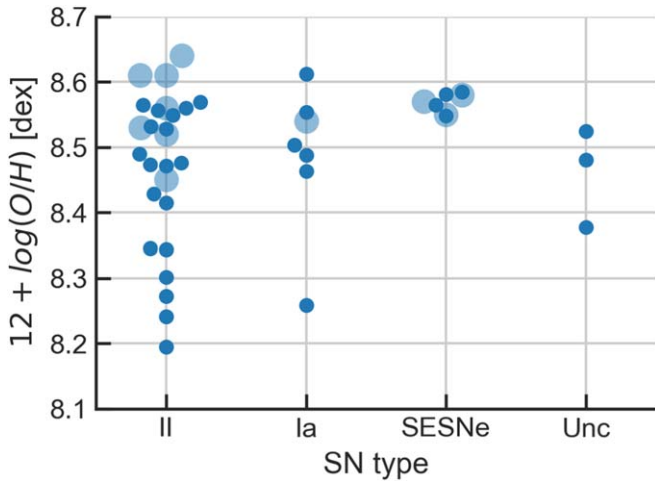


**Figure 11.** Estimated metallicity values at each SN site based on Groves et al. (2023). The small circles plot estimates of metallicity based on radial gradients. The large, transparent circles show estimates for the specific H II region coincident with the SN. Both estimates use the Scal system. We separate the sample by SN type.

“Scal” metallicity estimates (Pilyugin & Grebel 2016) for individual H II regions. We also plot the specific metallicity values estimated at individual H II regions for the subset of SNe within an H II region.

3. *Velocity dispersion measured from ionized gas ( $\sigma$ ):* The velocity dispersion estimated from the ionized gas may give a clue as to whether  $H\alpha$  emission is coming from an H II region or shocks, e.g., driven by winds or even the SN itself due to late-time CSM interactions. We therefore also record the velocity dispersion ( $\sigma$ ) of the  $H\alpha$  emission at each SN site. None of our SN samples show signs of broadening with  $\sigma \gg 100 \text{ km s}^{-1}$ .

The nebulae coincident with our SNe appear consistent with normal H II regions. The metallicities that we record are informational and potentially of use in broader future studies, such as determining the metallicity dependence on the rates of individual SN types (e.g., Pessi et al. 2023). Our own sample lacks a wide range in metallicity and the heterogeneous nature of our SN compilation makes it poorly suited to study SN rates.

## 5. Discussion and Summary

We have analyzed the coincidence of recent ( $\lesssim 125$  yr old) SNe with  $H\alpha$  emission in the PHANGS–MUSE survey (Emsellem et al. 2022). Within the 19 PHANGS–MUSE targets, we identify 32 SNe in 10 galaxies that lie within the footprint of the MUSE observations and meet our criteria for being included within our sample.

1. We find that 41% (13/32) of the SNe within the PHANGS–MUSE footprint occur coincident with one of the H II regions identified by Groves et al. (2023; see Section 3.1 and Table 1). The majority of these SNe (11/13) are also coincident with CO (2–1) emission (Section 4.1).

We construct a series of models to test how much of this SNe–H II region overlap may result from chance alignment (Section 2.3).

2. Based on controls using the near-IR emission from the galaxy or considering random placement within a 500–1000 pc sized region around the SNe, many of the

SNe found coincident with H II regions are likely to be associated by chance. Overall, by chance alone, we would expect  $\approx 1/3$  of SNe to appear associated with H II regions for our targets and the MUSE resolution. This reflects that core-collapse SNe tend to occur in regions of galaxies with a high density of star formation activity (Section 3.1).

3. Examining the SN locations in new high-resolution HST narrowband  $H\alpha$  imaging (Chandar, A. Barnes et al. 2024, in preparation) confirms that SNe tend to explode *near* but not directly *in* H II regions traced by  $H\alpha$  (Section 3.6).
4. After accounting for this chance overlap, our best estimate is that  $\approx 19.2\% \pm 10.4\%$  of CCSNe occur within and are associated with an H II region (Section 3.1). Consistent with other recent work, this low percentage implies a large role for stellar winds, photoionized gas pressure, and radiation pressure (i.e., “pre-SN” feedback) in clearing gas away from young stellar populations. It also implies that SNe are more likely to explode into lower-density regions and thus affect a larger physical area (e.g., Chevance et al. 2020; Mayker Chen et al. 2023; Sarbadhicary et al. 2023).

We validate this result by analyzing intensity statistics and the distance from each SN to the nearest H II region (Sections 3.4 and 3.5). SNe Ia, which originate from older progenitors, show a closer association with the older stellar population compared to core-collapse SNe. By contrast, stripped-envelope SNe (SNe Ib/c), which are believed to originate from high-mass stars, show the most direct association with  $H\alpha$  emission and H II regions out of our sample (Section 3.2). These results by type are in good agreement with previous lower-resolution work on larger samples (including James & Anderson 2006; Anderson et al. 2012; Crowther 2013; Galbany et al. 2014).

In addition to  $H\alpha$  intensity, we examine extinction and other properties of the nebular regions associated with SNe.

5. The Balmer decrement implies extinction toward the ionized gas near SNe of  $A_V \approx 0\text{--}2.35$  mag. We find no strong differences between the overall  $A_V$  values in the PHANGS–MUSE maps and those at the sites of SNe. This appears consistent with modestly measured  $A_V$  toward core-collapse SNe in normal star-forming galaxies (Section 4.2).

Thanks to ASAS-SN, ATLAS, the Zwicky Transient Facility, and the upcoming Rubin LSST, we are in the era of high completeness SNe discovery toward nearby galaxies. Therefore we expect the kind of detailed, high-physical-resolution studies presented here and in Mayker Chen et al. (2023) to become increasingly possible and informative. We note two conclusions relevant to such next steps:

6. High physical resolution, of order 10 pc, is needed to isolate SNe within individual clouds or H II regions. Given that core-collapse SNe often occur in complex regions of galaxies with active star formation, there is a larger possibility of accidental alignment at coarser resolutions. This is also of order the resolution needed to resolve the likely cooling radius (and so the zone of influence) of SN explosions (e.g., Kim & Ostriker 2015; Martizzi et al. 2015).

7. To achieve such high resolution, correspondingly high accuracy in the localization of SNe is required. Practically, to make the best use of space telescopes or ALMA for such studies, SNe must be localized to better than  $\pm 0''.1$ .

With these caveats in mind, the future in this area looks bright. JWST, HST, ALMA, and soon Euclid and Roman offer amazing prospects to localize SNe in the nearest galaxies and better understand the impact and origin of these explosions.

### Acknowledgments

N.M.C. thanks the Ohio State University's Galaxy and Supernova groups, including Christopher Kochanek, for useful discussions at several stages of the project. This work was carried out as part of the PHANGS collaboration.

Support for this work was provided by the NSF through the award SOSP SOSPADA-010 from the NRAO, which supported the work of N.M.C. The work of N.M.C. and A.K.L. was partially supported by the National Science Foundation (NSF) under grants Nos. 1615105, 1615109, and 1653300.

The work of A.K.L. is partially supported by the National Aeronautics and Space Administration (NASA) under ADAP grants NNX16AF48G and NNX17AF39G. K.G. is supported by the Australian Research Council through the Discovery Early Career Researcher Award (DECRA) Fellowship (project No. DE220100766) funded by the Australian Government.

K.K., J.E.M.D., and O.V.E. gratefully acknowledge funding from the Deutsche Forschungsgemeinschaft (DFG, German Research Foundation) in the form of an Emmy Noether Research Group (grant No. KR4598/2-1, PI Kreckel) and the European Research Council's starting grant ERC StG-101077573 ("ISM-METALS").

M.C. gratefully acknowledges funding from the Deutsche Forschungsgemeinschaft (DFG, German Research Foundation) through an Emmy Noether Research Group (grant No. CH2137/1-1). COOL Research DAO is a Decentralized Autonomous Organization supporting research in astrophysics aimed at uncovering our cosmic origins.

This paper makes use of the PHANGS–MUSE data, based on observations collected at the European Southern Observatory under ESO programs 094.C-0623 (PI: Kreckel), 095.C-0473, 098.C-0484 (PI: Blanc), 1100.B-0651 (PHANGS–MUSE; PI: Schinnerer), as well as 094.B-0321 (MAGNUM; PI: Marconi), 099.B-0242, 0100.B-0116, 098.B-0551 (MAD; PI: Carollo) and 097.B-0640 (TIMER; PI: Gadotti).

This paper makes use of the following ALMA data, which have been processed as part of the PHANGS–ALMA CO (2–1) survey: ADS/JAO.ALMA#2012.1.00650.S ADS/JAO.

ALMA#2013.1.00803.S ADS/JAO.ALMA#2013.1.01161.S ADS/JAO.ALMA#2015.1.00121.S ADS/JAO.ALMA#2015.1.00782.S ADS/JAO.ALMA#2015.1.00925.S ADS/JAO.ALMA#2015.1.00956.S ADS/JAO.ALMA#2016.1.00386.S ADS/JAO.ALMA#2017.1.00392.S ADS/JAO.ALMA#2017.1.00766.S ADS/JAO.ALMA#2017.1.00886.L ADS/JAO.ALMA#2018.1.00484.S ADS/JAO.ALMA#2018.1.01321.S ADS/JAO.ALMA#2018.1.01651.S ADS/JAO.ALMA#2018.A.00062.S ADS/JAO.ALMA#2019.1.01235.S ADS/JAO.ALMA#2019.2.00129.S ALMA is a partnership of ESO (representing its member states), NSF (USA), and NINS (Japan), together with NRC (Canada), NSC and ASIAA (Taiwan), and KASI (Republic of Korea), in cooperation with the Republic of Chile. The Joint ALMA Observatory is operated by ESO, AUI/NRAO, and NAOJ. The National Radio Astronomy Observatory (NRAO) is a facility of NSF operated under a cooperative agreement by Associated Universities, Inc (AUI).

This research is based on observations made with the NASA/ESA Hubble Space Telescope obtained from the Space Telescope Science Institute, which is operated by the Association of Universities for Research in Astronomy, Inc., under NASA contract NAS 526555. These observations are associated with program 15654.

This work has made use of the Transient Name Server, provided by the IAU supernova working group, last accessed on 2023 December 30, which included observations and metadata for over 140,000 astronomical transients.

This work acknowledges the Open Supernova Catalog (OSC; Guillochon et al. 2017), last accessed on 2022 January 26th, which included observations and metadata for  $\sim 80,000$  SNe and SNRs.

This work has made use of the SAO/NASA Astrophysics Data System, the NASA/IPAC Extragalactic Database (NED), which is operated by the Jet Propulsion Laboratory, California Institute of Technology, under contract with the National Aeronautics and Space Administration, the SIMBAD database, operated at CDS, Strasbourg, France, and the Central Bureau for Astronomical Telegrams (CBAT) and the International Astronomical Union Circulars (IAUC) catalog, operated at Harvard College Observatory, Cambridge, Massachusetts.

This work has utilized the following software: Jupyter (Kluyver et al. 2016), Astropy (Astropy Collaboration et al. 2013, 2018), Pandas (McKinney 2010), NumPy (van der Walt et al. 2011; Harris et al. 2020), SciPy (Virtanen et al. 2020), Seaborn (Waskom et al. 2017), Matplotlib (Hunter 2007), and GitHub (github 2020).

## Appendix

In Table A1, we list the recent SN that occur in the footprint of the MUSE galaxy sample. Table A1 lists the SN name, host galaxy, type, right ascension and declination, whether each is included in our project sample, and the reference paper used for the type classification. In Table A2, we report specific measurements pertaining to each SN in our sample. This includes the SN's type classification, native Ha map resolution, Ha intensity measured at the SN site, the velocity dispersion, extinction, H II region status,

BPT diagnostic line classifications, presence of CO (2–1) emission, directly measured H II region metallicities (when available), and calculated metallicities using galaxy gradients, galactocentric radius, and effective radius of each SN site. Figures A1–A3 show PHANGS—MUSE Ha emission cutouts ( $500 \times 500$  pc) centered on the locations of the SNe in our sample. Figures A4–A9 compare the PHANGS—MUSE Ha emission cutouts (left panels) with HST (right panels) Ha emission cutouts of the same size ( $500 \times 500$  pc) centered on the locations of the SNe in our sample.

**Table A1**  
Supernovae in MUSE Galaxies

Galaxy	Supernova	Type	R.A.	Decl.	In Sample	References
NGC 0628	SN2013ej	II	24.2007	15.7586	...	Leonard et al. (2013)
NGC 0628	SN2019krl	IIn/LBV	24.2068	15.7795	...	Andrews et al. (2021)
NGC 1087	SN1995V	II	41.6115	−0.4988	✓	Evans et al. (1995)
NGC 1300	SN2022acko	II	49.9125	−19.3952	✓	Li et al. (2022)
NGC 1365	SN1957C	Unclassified	53.3835	−36.1177	✓	HAC 1383
NGC 1365	SN1983V	Ib	53.3819	−36.1486	✓	Wheeler et al. (1987)
NGC 1365	SN2001du	II	53.3713	−36.1421	✓	Smartt et al. (2001)
NGC 1365	SN2012fr	Ia	53.4006	−36.1268	✓	Klotz et al. (2012)
NGC 1433	SN1985P	II	55.5264	−47.21	✓	Kirshner et al. (1985)
NGC 1566	ASASSN-14ha	II	65.0059	−54.9381	✓	Arcavi et al. (2014)
NGC 1566	SN2010el	Ia-02cx	64.9951	−54.944	✓	Bessell & Schmidt (2010)
NGC 1566	SN2021aefx	Ia	64.9725	−54.9481	✓	Valenti et al. (2021)
NGC 1672	SN2017gax	Ib/c	71.4561	−59.2451	...	Jha et al. (2017)
NGC 1672	SN2022aau	II	71.424	−59.2454	✓	Siebert & Foley (2022)
NGC 3627	SN1973R	II	170.0481	12.9977	✓	Ciatti & Rosino (1977)
NGC 3627	SN1989B	Ia	170.058	13.0053	✓	Marvin et al. (1989)
NGC 3627	SN1997bs	IIn	170.0593	12.9721	✓	Adams & Kochanek (2015)
NGC 3627	SN2009hd	II	170.0707	12.9796	✓	Kasliwal et al. (2009)
NGC 3627	SN2016cok	II P	170.0796	12.9824	✓	Zhang et al. (2016)
NGC 4254	SN1967H	II	184.7184	14.414	✓	Fairall (1967)
NGC 4254	SN1972Q	II	184.7107	14.4443	✓	Rosino (1972)
NGC 4254	SN1986I	II	184.7169	14.4123	✓	Pennypacker et al. (1986)
NGC 4254	SN2014L	Ic	184.7029	14.4121	✓	Yamaoka et al. (2014)
NGC 4303	SN1926A	II	185.4754	4.4934	✓	IAUC 111
NGC 4303	SN1961I	II	185.5018	4.4704	✓	Humason et al. (1962)
NGC 4303	SN1964F	II	185.4698	4.4738	✓	IAUC 1868
NGC 4303	SN1999gn	II P	185.4876	4.4627	✓	Ayani & Yamaoka (1999)
NGC 4303	SN2006ov	II	185.4804	4.488	✓	Blondin et al. (2006)
NGC 4303	SN2014dt	Ia Pec	185.4899	4.4718	✓	Ochner et al. (2014)
NGC 4303	SN2020jfo	II P	185.4602	4.4817	✓	Perley et al. (2020)
NGC 4321	SN1901B	I	185.6971	15.8238	✓	Tsvetkov & Bartunov (1993)
NGC 4321	SN1959E	I	185.7454	15.817	✓	Porter (1993)
NGC 4321	SN1979C	II	185.7442	15.7978	...	Carney (1980)
NGC 4321	SN2006X	Ia	185.7249	15.809	✓	Quimby et al. (2006)
NGC 4321	SN2019ehk	Ib	185.7339	15.8261	✓	De et al. (2021)
NGC 4321	SN2020oi	Ic	185.7289	15.8236	✓	Siebert et al. (2020)



**Table A2**  
Measurements from the Supernovae Sample

Supernova	Type	Resolution	Distance	$H_{\alpha}$	$\sigma$	$A_V$	H II	N II	S II	O I	CO	Metallicity	$R_{\text{gal}}$	$R_{\text{eff}}$
ASASSN-14 ha	II	0.8 (80)	17.69	621	57	0.86	Yes (877)	0.0	0.0	0.0	Yes	8.56 (8.61)	0.05	1.31
SN1901B	I	1.16 (43)	15.21	211	53	0.92	No (−1)	...	...	...	Yes	8.38	0.57	7.67
SN1926A	II	0.78 (73)	16.99	82	67	0.0	No (−1)	...	...	...	No	8.34	0.35	8.42
SN1957C	Unclassified	1.15 (76)	19.57	294	63	0.38	No (−1)	...	...	...	No	8.52	0.81	43.17
SN1959E	I	1.16 (43)	15.21	361	55	1.07	No (−1)	...	...	...	Yes	8.48	0.3	3.98
SN1961I	II	0.78 (73)	16.99	415	58	0.35	Yes (373)	0.0	0.0	0.0	No	8.3 (8.56)	0.4	9.73
SN1964F	II	0.78 (73)	16.99	29	59	0.0	No (−1)	...	...	...	No	8.49	0.16	3.85
SN1967H	II	0.89 (96)	13.1	1435	63	1.65	No (−1)	...	...	...	Yes	8.47	0.16	4.24
SN1972Q	II	0.89 (96)	13.1	362	56	0.78	No (−1)	...	...	...	Yes	8.27	0.43	11.34
SN1973R	II	1.05 (96)	11.32	1118	59	1.17	Yes (433)	0.0	0.0	0.0	Yes	8.56 (8.52)	0.29	4.39
SN1983V	Ic	1.15 (76)	19.57	1485	66	0.95	Yes (385)	0.0	0.0	0.0	Yes	8.58 (8.57)	0.48	25.77
SN1985P	II	0.91 (69)	18.63	25	67	0.24	No (−1)	...	...	...	No	8.47	0.35	7.37
SN1986I	II	0.89 (96)	13.1	515	62	0.52	No (−1)	...	...	...	Yes	8.48	0.15	4.08
SN1989B	Ia	1.05 (96)	11.32	1257	66	0.81	Yes (390)	0.0	0.0	0.0	Yes	8.55 (8.54)	0.17	2.58
SN1995V	II	0.92 (84)	15.85	884	52	1.28	Yes (731)	0.0	0.0	0.0	Yes	8.24 (8.45)	0.14	3.4
SN1997bs	IIn	1.05 (96)	11.32	99	55	0.78	Yes (961)	1.0	0.0	0.0	Yes	8.56 (nan)	0.24	3.66
SN1999gn	II P	0.78 (73)	16.99	1285	61	0.41	Yes (58)	0.0	0.0	0.0	Yes	8.43 (8.64)	0.24	5.76
SN2001du	II	1.15 (76)	19.57	135	68	0.18	No (−1)	...	...	...	No	8.53	0.79	41.99
SN2006X	Ia	1.16 (43)	15.21	37	60	0.54	No (−1)	...	...	...	No	8.5	0.24	3.17
SN2006ov	II	0.78 (73)	16.99	331	68	0.33	No (−1)	...	...	...	No	8.41	0.26	6.19
SN2009hd	II	1.05 (96)	11.32	3081	68	1.03	Yes (396)	0.0	0.0	0.0	Yes	8.56 (8.53)	0.2	3.0
SN2010el	Ia	0.8 (80)	17.69	38	68	0.26	No (−1)	...	...	...	Yes	8.49	0.13	3.39
SN2012fr	Ia	1.15 (76)	19.57	9	68	0.0	No (−1)	...	...	...	No	8.61	0.31	16.54
SN2014L	Ic	0.89 (96)	13.1	3366	63	1.47	Yes (1309)	0.0	0.0	0.0	Yes	8.53 (8.55)	0.08	2.08
SN2014dt	Ia Pec	0.78 (73)	16.99	90	71	0.28	No (−1)	...	...	...	No	8.46	0.19	4.69
SN2016cok	II P	1.05 (96)	11.32	518	62	1.36	No (−1)	...	...	...	Yes	8.57	0.35	5.22
SN2019ehk	Ib	1.16 (43)	15.21	104	76	1.47	Yes (1722)	1.0	0.0	0.0	No	8.55 (nan)	0.12	1.59
SN2020jfo	II P	0.78 (73)	16.99	220	57	0.92	No (−1)	...	...	...	No	8.35	0.35	8.37
SN2020oi	Ic	1.16 (43)	15.21	5473	66	1.01	Yes (1693)	0.0	0.0	0.0	Yes	8.58 (8.58)	0.02	0.28
SN2021aefx	Ia	0.8 (80)	17.69	13	73	0.0	No (−1)	...	...	...	No	8.26	0.35	9.59
SN2022aau	II	0.96 (104)	19.4	9695	76	2.35	Yes (803)	0.0	0.0	0.0	Yes	8.55 (8.61)	0.05	1.32
SN2022acko	II	0.89 (83)	18.99	34	66	0.3	No (−1)	...	...	...	No	8.19	0.38	5.35

**Note.** Resolution in arcseconds (pc), distance in Mpc, extinction-corrected  $H_{\alpha}$  intensity in flux units of  $10^{37} \text{ erg s}^{-1} \text{ kpc}^{-2}$ ,  $\sigma$  ( $H_{\alpha}$  velocity dispersion, corrected for instrumental broadening) in units of  $\text{km s}^{-1}$ ,  $A_V$  derived using the Balmer decrement (Groves et al. 2023), adopting  $R_V = 3.1$  and an O'Donnell (1994) extinction curve, H II regions identified in Groves et al. (2023), N II, S II, O I BPT emission line diagnostics taken from Groves et al. (2023), CO (2–1) detection assigned when signal-to-noise  $\geq 3$  from PHANGS–ALMA broad moment-0 maps (Leroy et al. 2021), metallicity in  $[12+\log(\text{O}/\text{H})]$  (dex) calculated using the galactic metallicity gradient, determined using  $\text{Sc} \text{II}$  metallicities, and the galactocentric radius of each SN (empirical values from Groves et al. 2023 when available),  $R_{\text{gal}}$  in kpc.

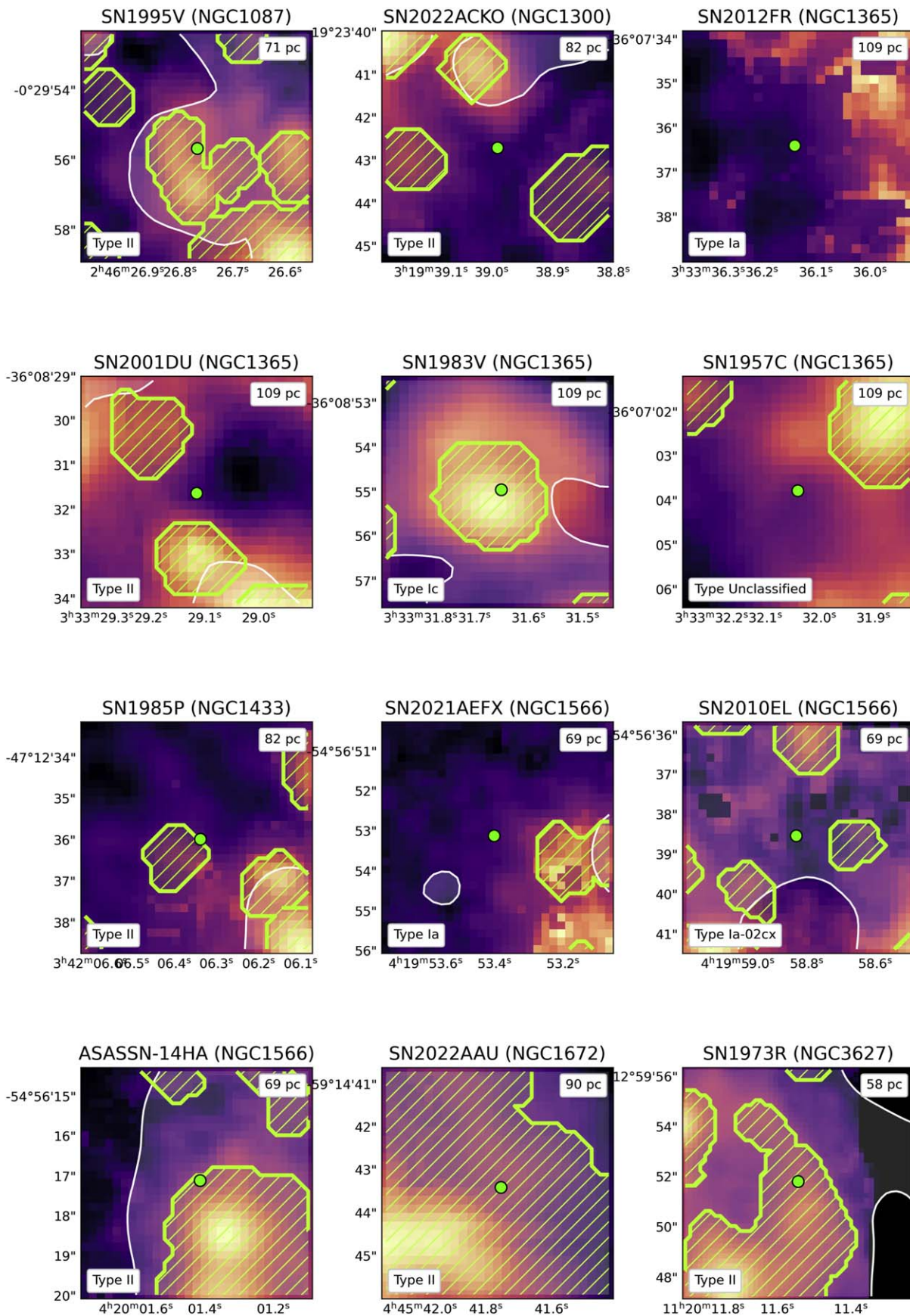


**Figure A1.** PHANGS-MUSE  $H\alpha$  emission cutouts (500  $\times$  500 pc) centered on the locations of the SNe in our sample. Each galaxy is plotted at its native resolution, listed in the top right corner. Lime contours enclose H II regions identified by Groves et al. (2023). SNe are marked with white circles. In the legend, SNe are labeled with their type classification. Each panel is oriented with the top of the figure as north; east is left.

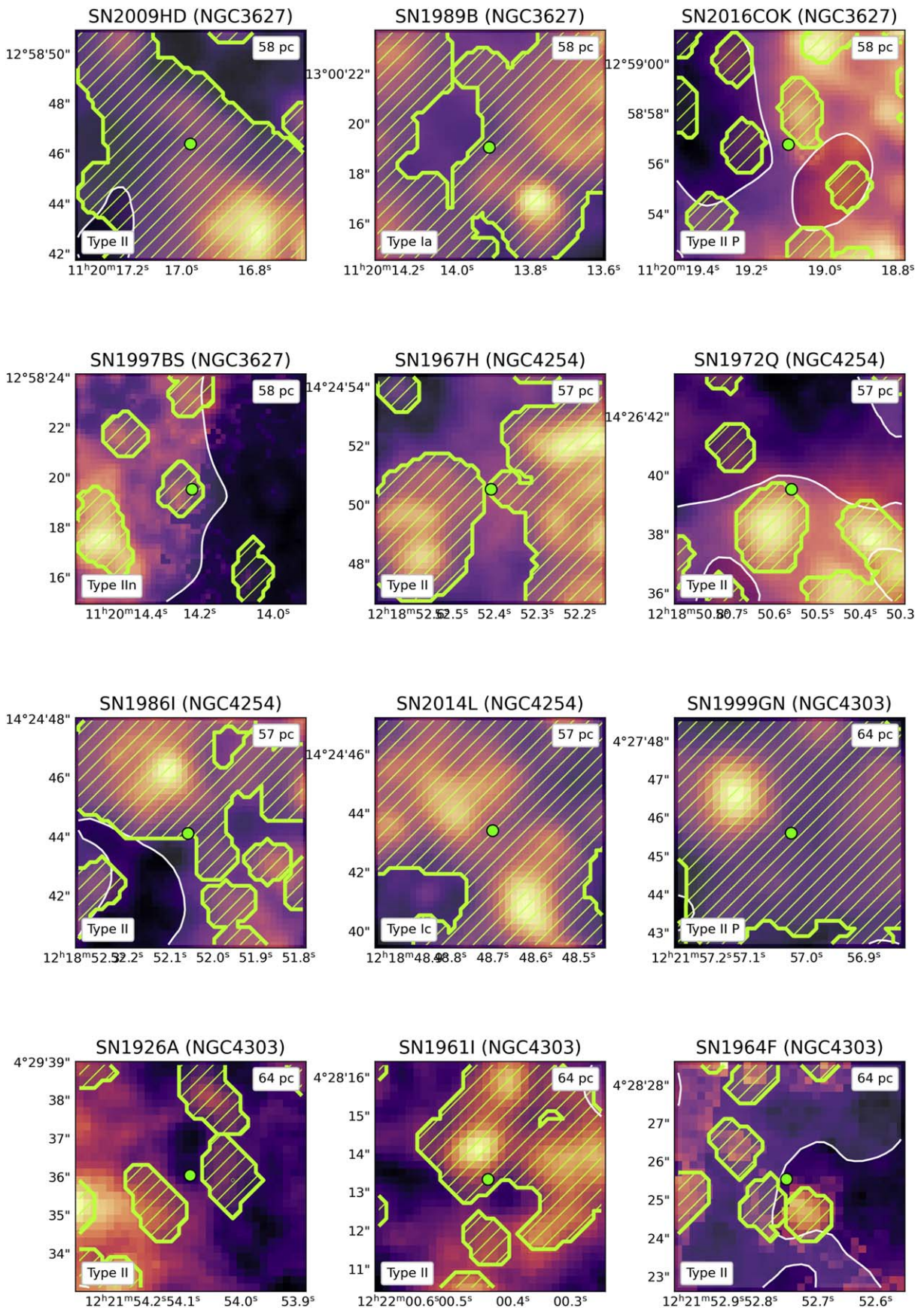


Figure A2. Figure A1 continued.

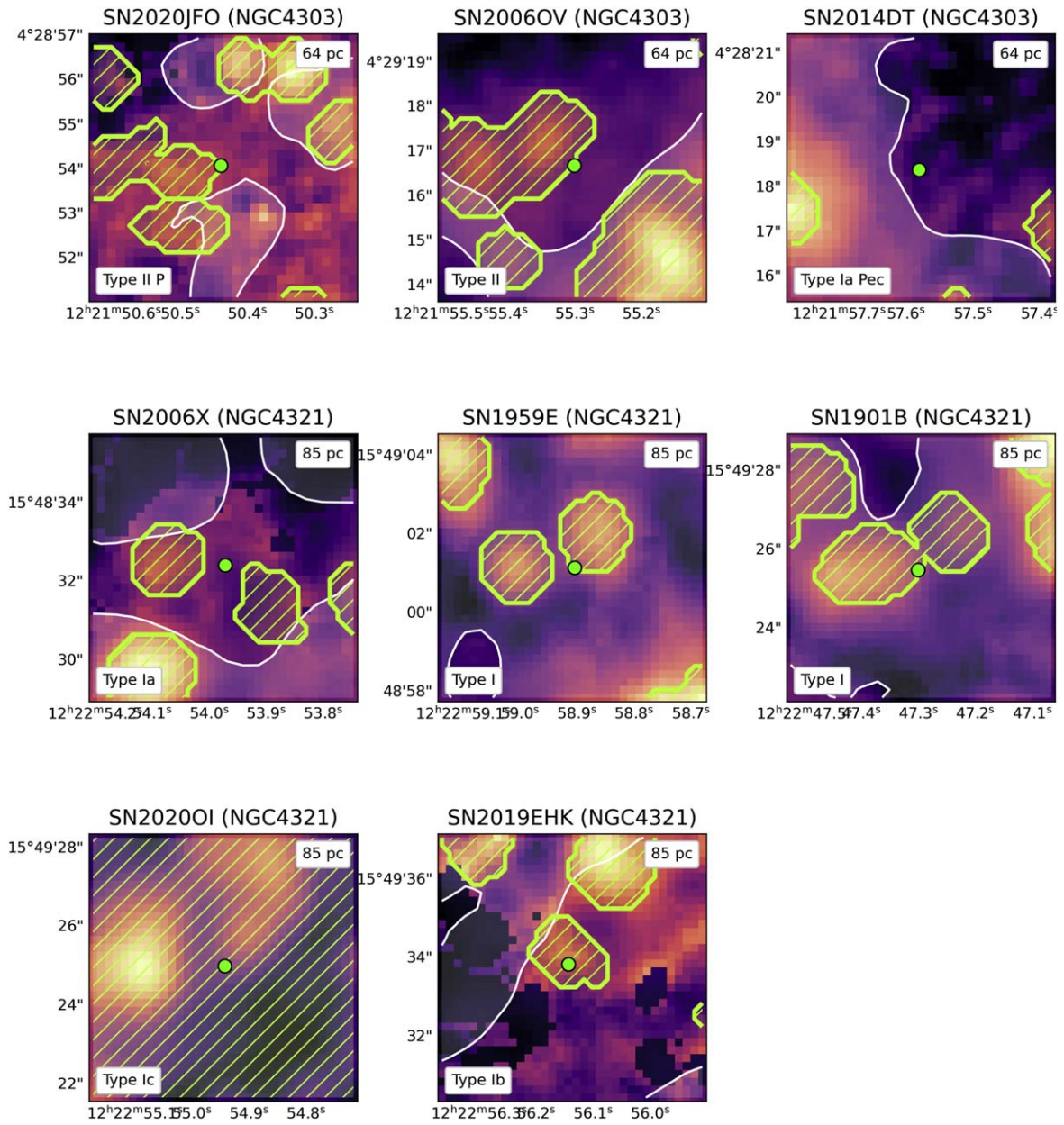
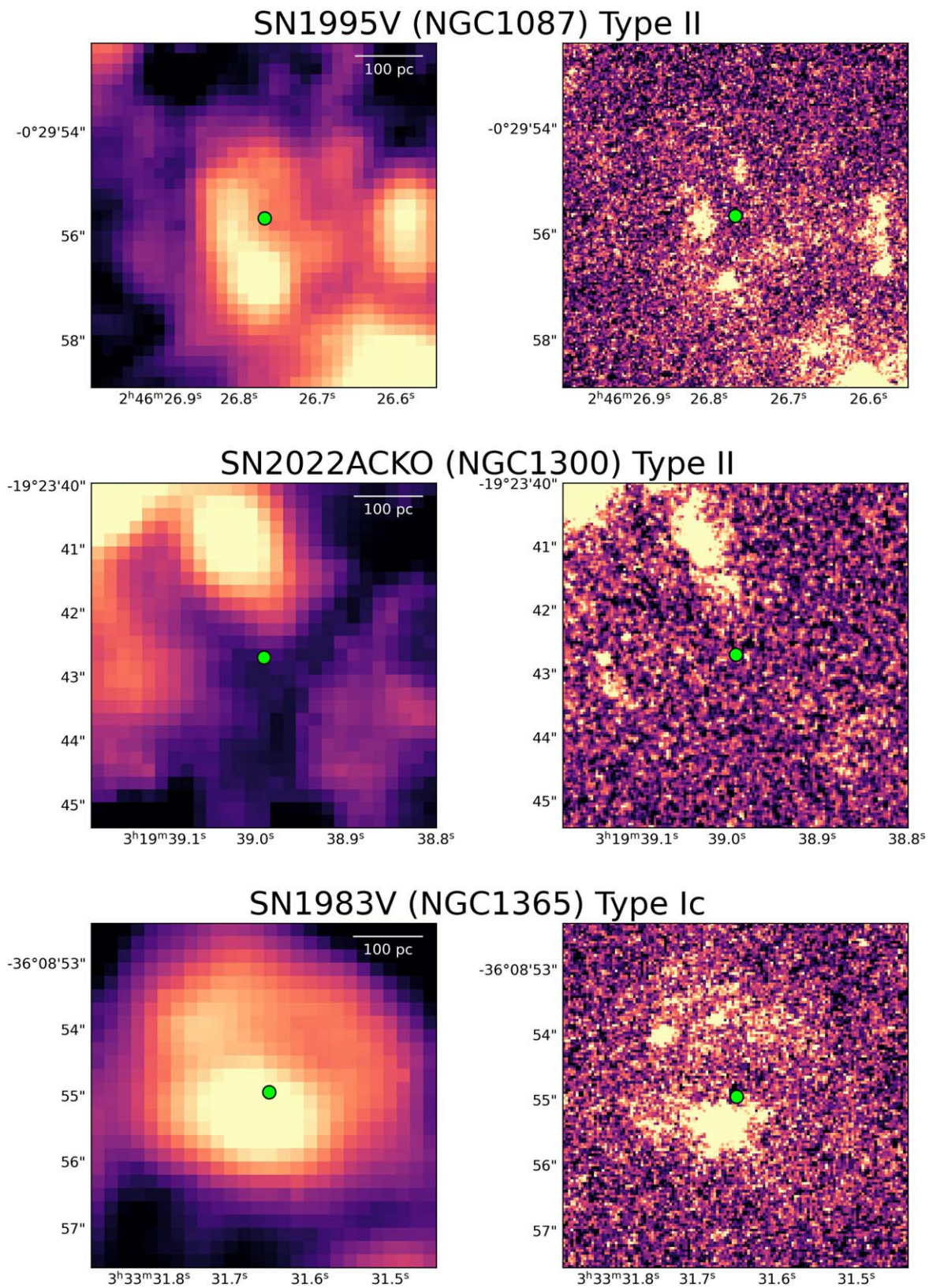
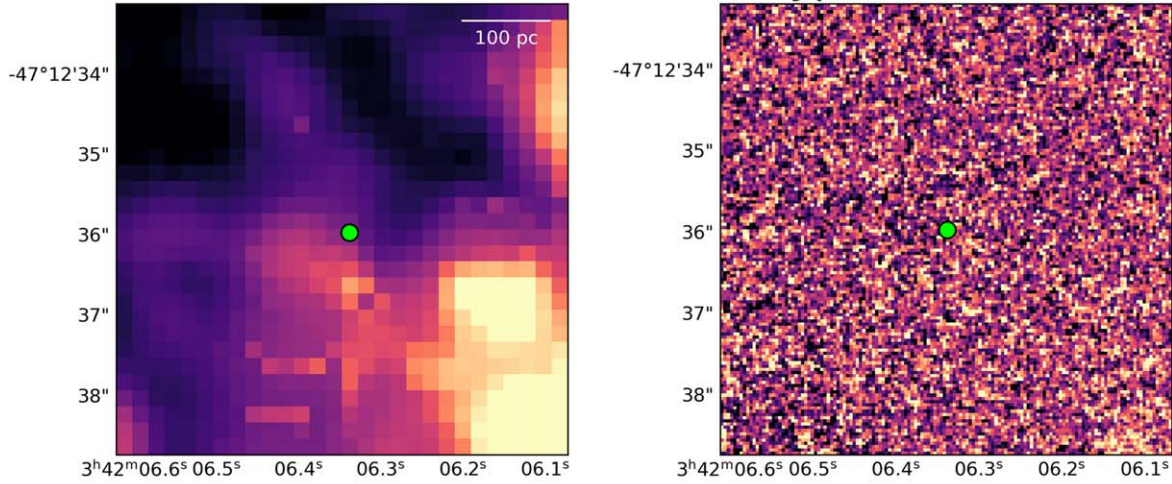


Figure A3. Figure A1 continued.

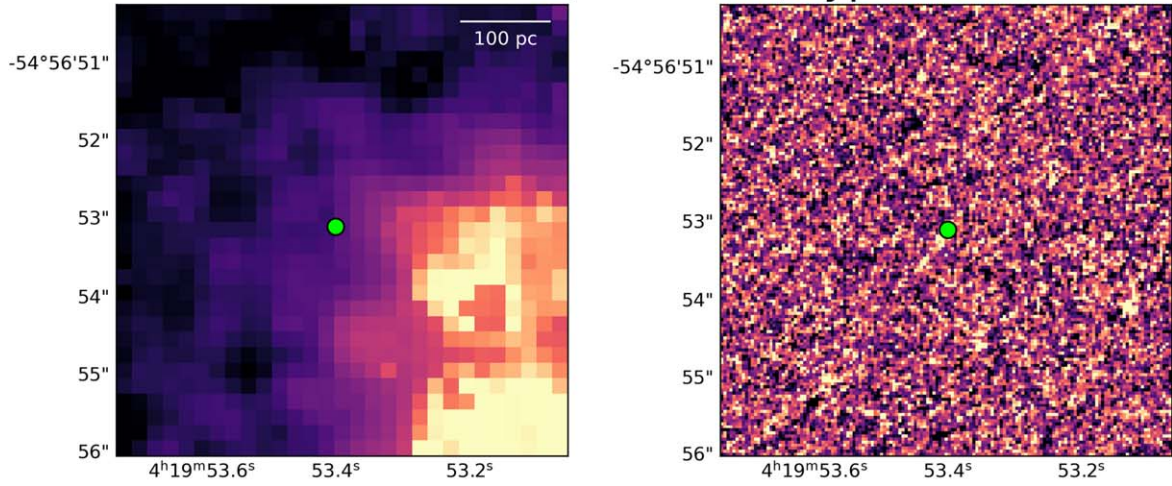


**Figure A4.** Comparison of PHANGS–MUSE (left panels) and HST (right panels)  $H\alpha$  emission cutouts ( $500 \times 500$  pc) centered on the locations of the SNe in our sample. SNe are marked with green circles. SNe are labeled with their host galaxy and type classification in the title of each subplot row. Each panel is oriented with the top of the figure as north; east is left.

### SN1985P (NGC1433) Type II



### SN2021AEFX (NGC1566) Type Ia



### SN2010EL (NGC1566) Type Ia-02cx

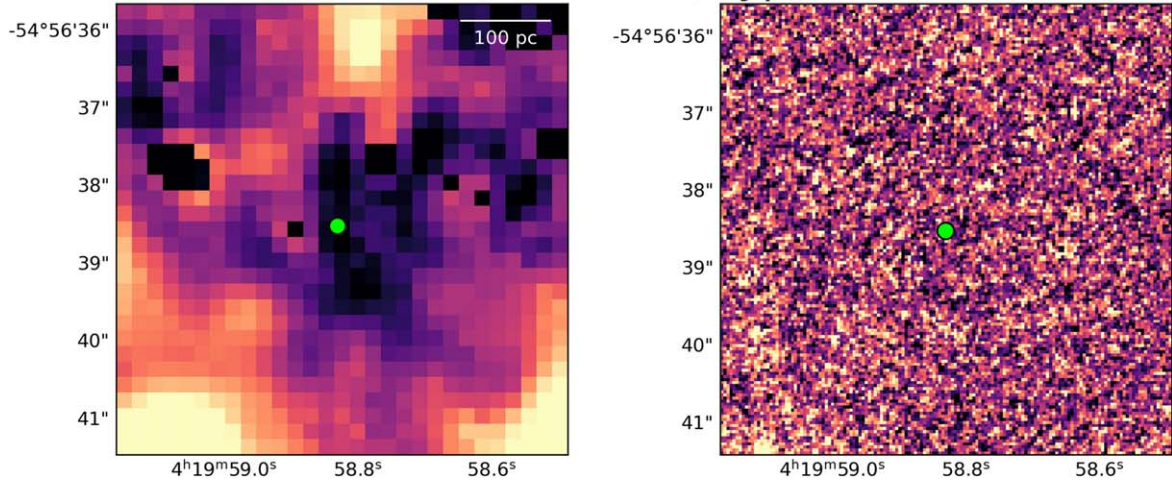
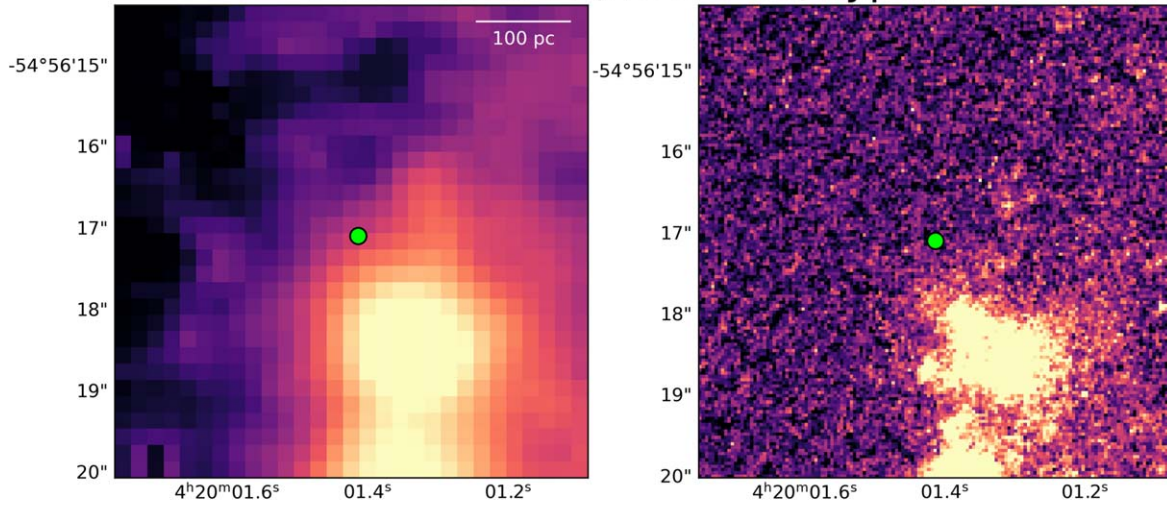


Figure A5. Figure A4 continued.

### ASASSN-14HA (NGC1566) Type II



### SN2022AAU (NGC1672) Type II

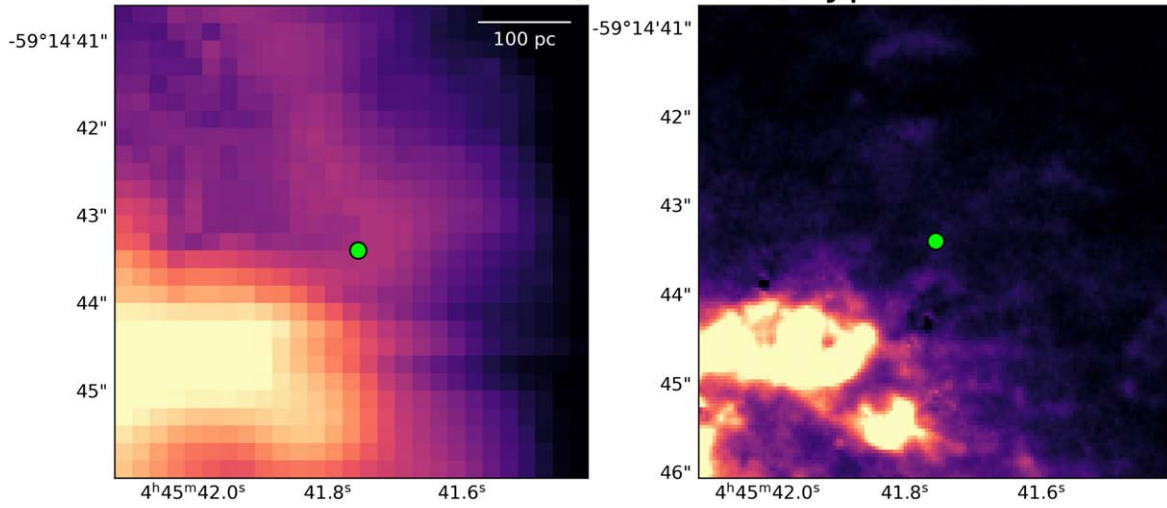
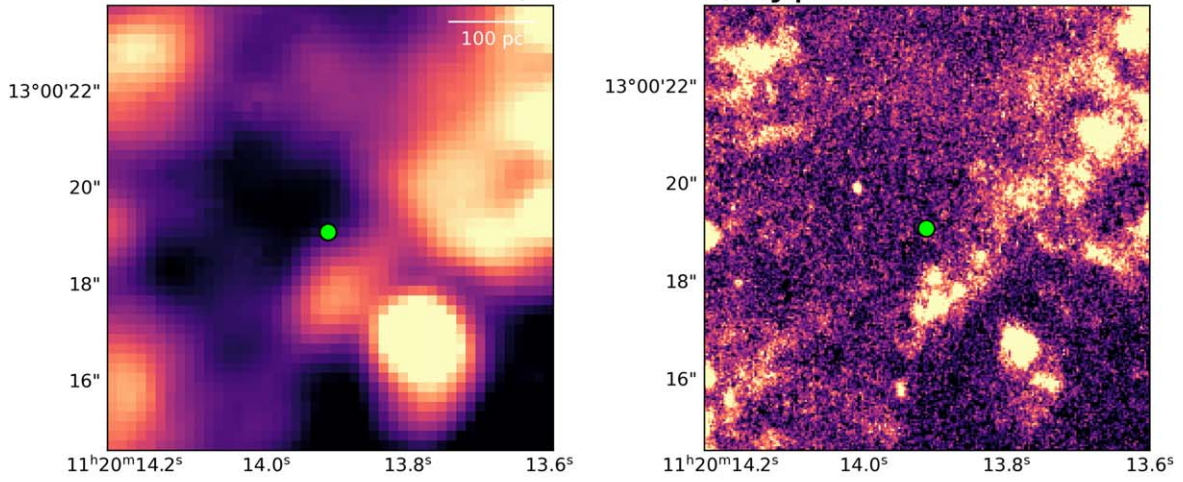
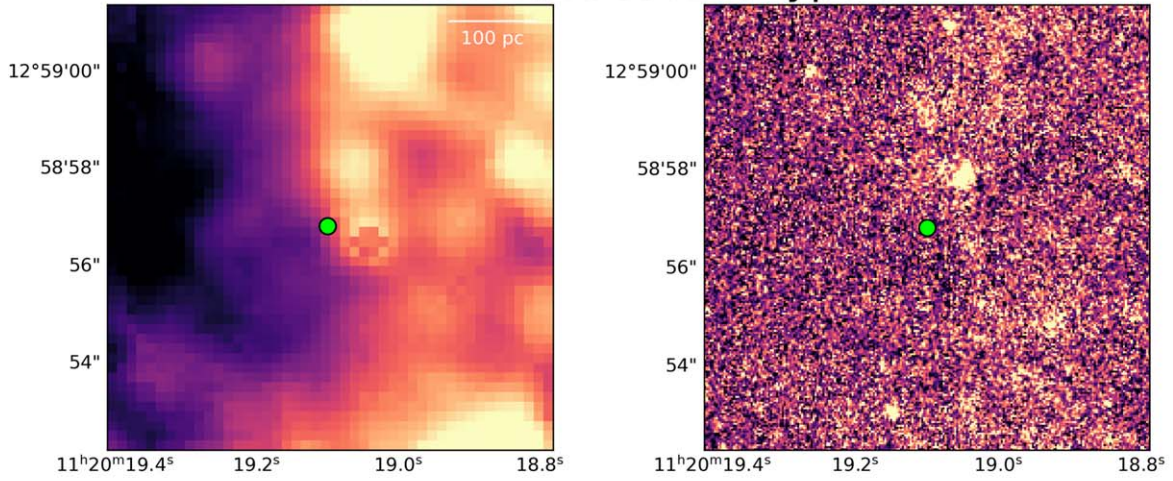


Figure A6. Figure A4 continued.

### SN1989B (NGC3627) Type Ia



### SN2016COK (NGC3627) Type II P



### SN2009HD (NGC3627) Type II

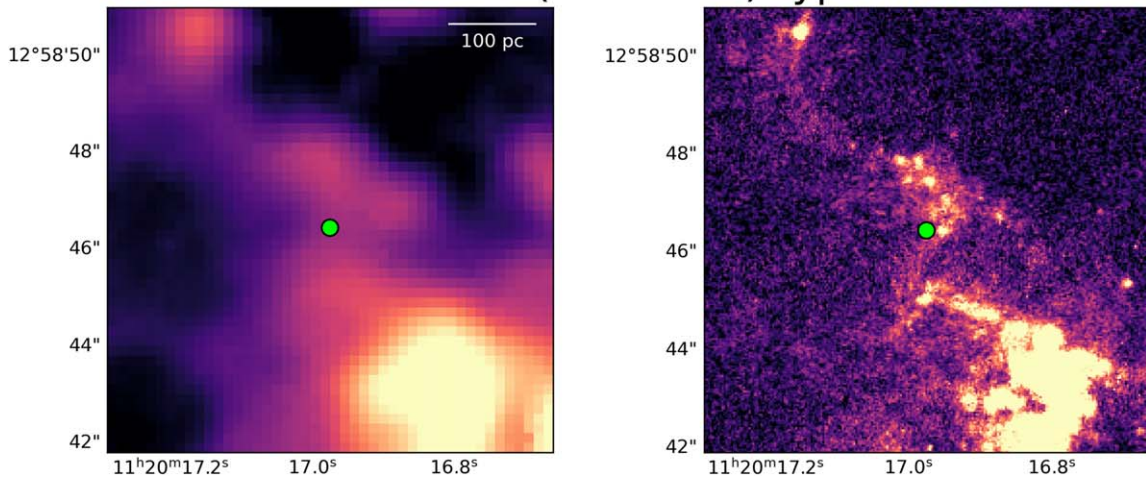
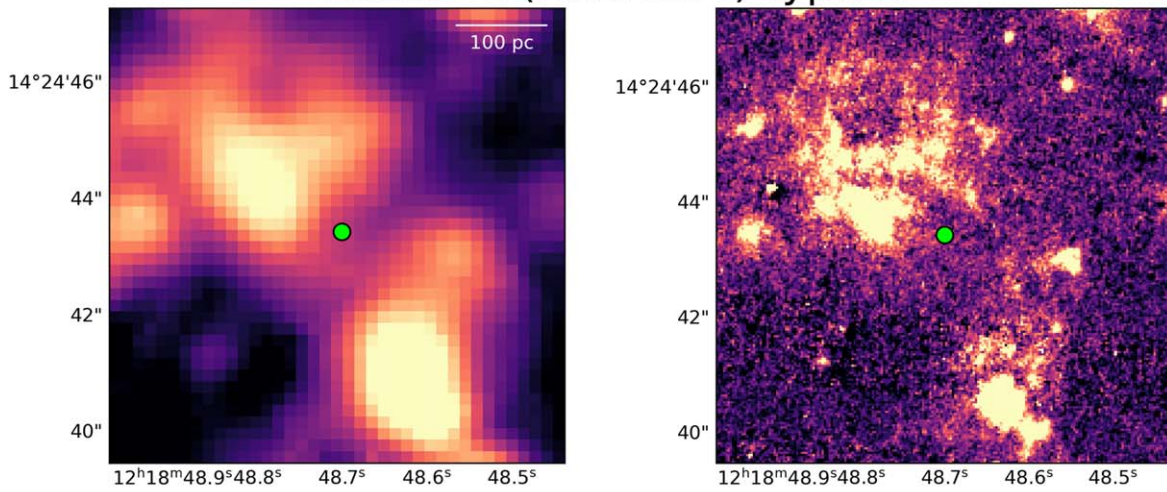


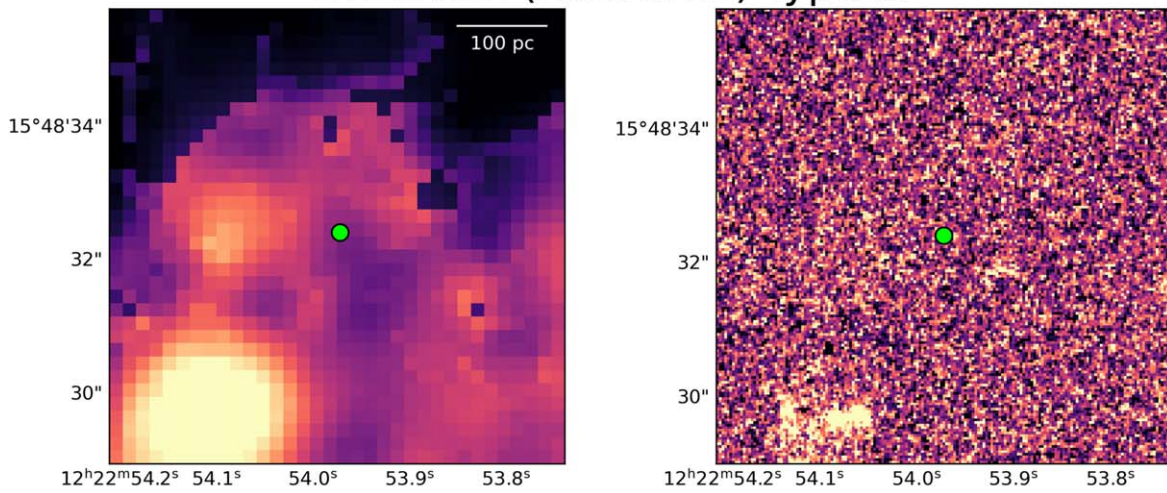
Figure A7. Figure A4 continued.



### SN2014L (NGC4254) Type Ic



### SN2006X (NGC4321) Type Ia



### SN1959E (NGC4321) Type I

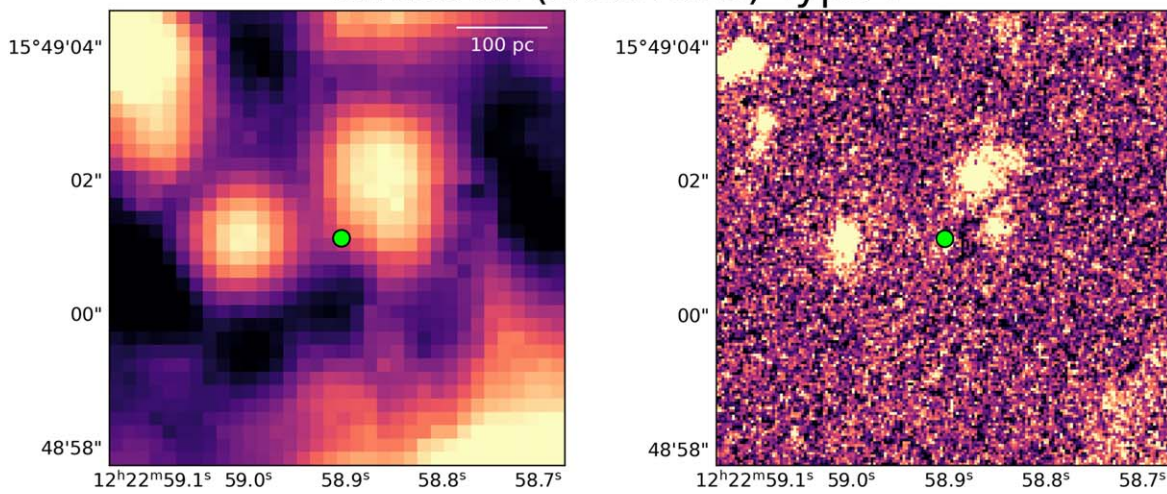
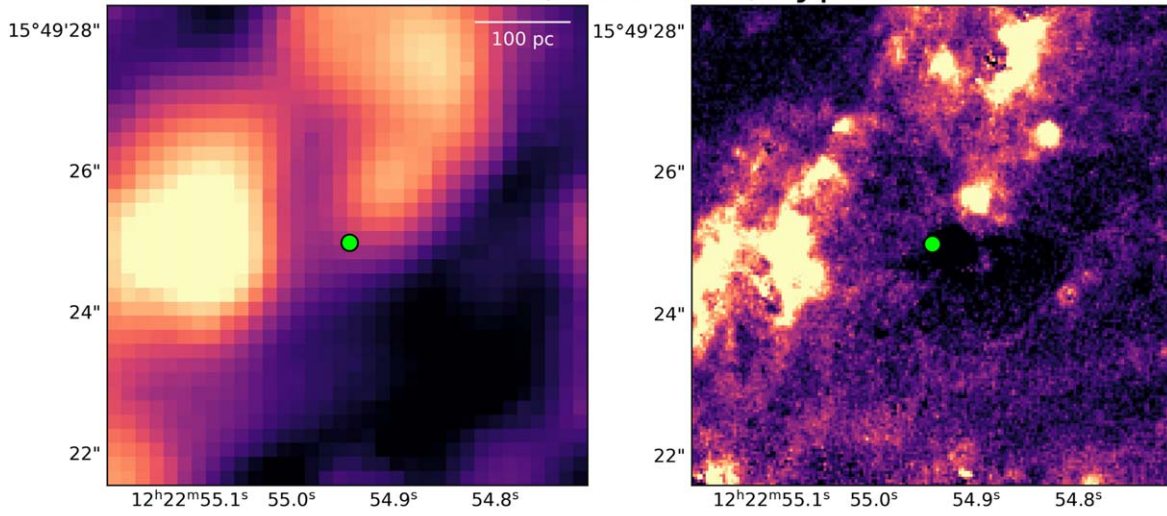


Figure A8. Figure A4 continued.

### SN2020OI (NGC4321) Type Ic



### SN2019EHK (NGC4321) Type Ib

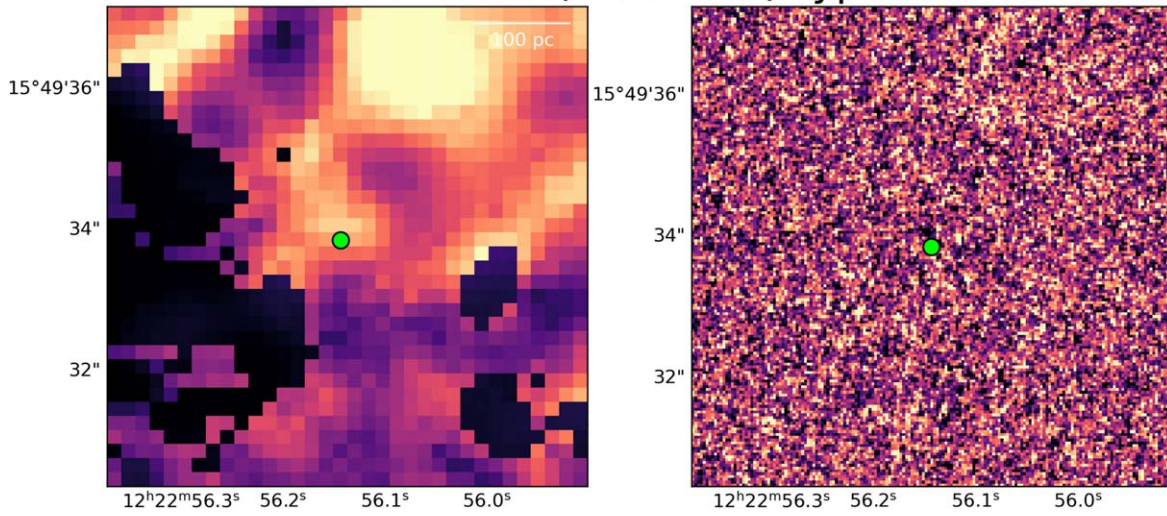


Figure A9. Figure A4 continued.

## ORCID iDs

Ness Mayker Chen  <https://orcid.org/0000-0002-5993-6685>  
 Adam K. Leroy  <https://orcid.org/0000-0002-2545-1700>  
 Sumit K. Sarbadhichary  <https://orcid.org/0000-0002-4781-7291>  
 Laura A. Lopez  <https://orcid.org/0000-0002-1790-3148>  
 Todd A. Thompson  <https://orcid.org/0000-0003-2377-9574>  
 Ashley T. Barnes  <https://orcid.org/0000-0003-0410-4504>  
 Eric Emsellem  <https://orcid.org/0000-0002-6155-7166>  
 Brent Groves  <https://orcid.org/0000-0002-9768-0246>  
 Rupali Chandar  <https://orcid.org/0000-0003-0085-4623>  
 Mélanie Chevance  <https://orcid.org/0000-0002-5635-5180>  
 Ryan Chown  <https://orcid.org/0000-0001-8241-7704>  
 Daniel A. Dale  <https://orcid.org/0000-0002-5782-9093>  
 Oleg V. Egorov  <https://orcid.org/0000-0002-4755-118X>  
 Simon C. O. Glover  <https://orcid.org/0000-0001-6708-1317>  
 Kathryn Grasha  <https://orcid.org/0000-0002-3247-5321>  
 Ralf S. Klessen  <https://orcid.org/0000-0002-0560-3172>  
 Kathryn Kreckel  <https://orcid.org/0000-0001-6551-3091>  
 Jing Li  <https://orcid.org/0000-0002-4825-9367>  
 J. Eduardo Méndez-Delgado  <https://orcid.org/0000-0002-6972-6411>  
 Eric J. Murphy  <https://orcid.org/0000-0001-7089-7325>  
 Debosmita Pathak  <https://orcid.org/0000-0003-2721-487X>  
 Eva Schinnerer  <https://orcid.org/0000-0002-3933-7677>  
 David A. Thilker  <https://orcid.org/0000-0002-8528-7340>  
 Leonardo Úbeda  <https://orcid.org/0000-0001-7130-2880>  
 Thomas G. Williams  <https://orcid.org/0000-0002-0012-2142>

## References

- Adams, S. M., & Kochanek, C. S. 2015, *MNRAS*, **452**, 2195  
 Anderson, J. P. 2014, in IAU Symp. 296, *Supernova Environmental Impacts*, ed. A. Ray & R. A. McCray (Cambridge: Cambridge Univ. Press), 121  
 Anderson, J. P., Habbergham, S. M., James, P. A., & Hamuy, M. 2012, *MNRAS*, **424**, 1372  
 Anderson, J. P., James, P. A., Förster, F., et al. 2015a, *MNRAS*, **448**, 732  
 Anderson, J. P., James, P. A., Habbergham, S. M., Galbany, L., & Kuncarayakti, H. 2015b, *PASA*, **32**, e019  
 Andrews, J. E., Jencson, J. E., Van Dyk, S. D., et al. 2021, *ApJ*, **917**, 63  
 Arcavi, I., Valenti, S., Hosseinzadeh, G., et al. 2014, *ATel*, **6466**, 1  
 Astropy Collaboration, Price-Whelan, A. M., Sipőcz, B. M., et al. 2018, *AJ*, **156**, 123  
 Astropy Collaboration, Robitaille, T. P., Tollerud, E. J., et al. 2013, *A&A*, **558**, A33  
 Audcent-Ross, F. M., Meurer, G. R., Audcent, J. R., et al. 2020, *MNRAS*, **492**, 848  
 Ayani, K., & Yamaoka, H. 1999, *IAUC*, **7336**, 1  
 Bacon, R., Accardo, M., Adjali, L., et al. 2010, *Proc. SPIE*, **7735**, 773508  
 Bagetakos, I., Brinks, E., Walter, F., et al. 2011, *AJ*, **141**, 23  
 Baldwin, J. A., Phillips, M. M., & Terlevich, R. 1981, *PASP*, **93**, 5  
 Barnes, A. T., Chandar, R., Kreckel, K., et al. 2022, *A&A*, **662**, L6  
 Barnes, A. T., Longmore, S. N., Dale, J. E., et al. 2020, *MNRAS*, **498**, 4906  
 Barnes, A. T., Watkins, E. J., Meidt, S. E., et al. 2023, *ApJL*, **944**, L22  
 Belfiore, F., Leroy, A. K., Sun, J., et al. 2023, *A&A*, **670**, A67  
 Belfiore, F., Santoro, F., Groves, B., et al. 2022, *A&A*, **659**, A26  
 Bessell, M. S., & Schmidt, B. P. 2010, *CBET*, **2337**, 1  
 Blondin, S., Modjaz, M., Kirshner, R., Challis, P., & Berlind, P. 2006, *CBET*, **757**, 1  
 Bolatto, A. D., Wolfire, M., & Leroy, A. K. 2013, *ARA&A*, **51**, 207  
 Calzetti, D. 2001, *PASP*, **113**, 1449  
 Carney, B. W. 1980, *PASP*, **92**, 56  
 Chevance, M., Kruijssen, J. M. D., Hygate, A. P. S., et al. 2020, *MNRAS*, **493**, 2872  
 Chevance, M., Kruijssen, J. M. D., Krumholz, M. R., et al. 2022, *MNRAS*, **509**, 272  
 Ciatti, F., & Rosino, L. 1977, *A&A*, **56**, 59  
 Cronin, S. A., Utomo, D., Leroy, A. K., et al. 2021, *ApJ*, **923**, 86  
 Crowther, P. A. 2013, *MNRAS*, **428**, 1927  
 De, K., Fremling, U. C., Gal-Yam, A., et al. 2021, *ApJL*, **907**, L18  
 Dessart, L., & Hillier, D. J. 2022, *A&A*, **660**, L9  
 Draine, B. T. 2011, *Physics of the Interstellar and Intergalactic Medium* (Princeton, NJ: Princeton Univ. Press)  
 Egorov, O. V., Kreckel, K., Glover, S. C. O., et al. 2023, *A&A*, **678**, A153  
 Eldridge, J. J. 2011, in ASP Conf. Ser. 440, *UP2010: Have Observations Revealed a Variable Upper End of the Initial Mass Function?*, ed. M. Treyer et al. (San Francisco, CA: ASP), 217  
 Elmegreen, B. 2004, in ASP Conf. Ser. 323, *Star Formation in the Interstellar Medium: In Honor of David Hollenbach*, ed. D. Johnstone et al. (San Francisco, CA: ASP), 117  
 Emsellem, E., Schinnerer, E., Santoro, F., et al. 2022, *A&A*, **659**, A191  
 Evans, R., & McNaught, R. H. 2003, *IAUC*, **8150**, 2  
 Evans, R. O., Jarman, J., Cragg, T., et al. 1995, *IAUC*, **6197**, 2  
 Fairall, A. P. 1967, *MNSSJ*, **26**, 148  
 Fox, O. D., Khandrika, H., Rubin, D., et al. 2021, *MNRAS*, **506**, 4199  
 Galbany, L., Mora, L., González-Gaitán, S., et al. 2017, *MNRAS*, **468**, 628  
 Galbany, L., Stanishev, V., Mourão, A. M., et al. 2014, *A&A*, **572**, A38  
 Gatto, A., Walch, S., Naab, T., et al. 2017, *MNRAS*, **466**, 1903  
 Girichidis, P., Walch, S., Naab, T., et al. 2016, *MNRAS*, **456**, 3432  
 github 2020, *GitHub*, <https://github.com/>  
 Groves, B., Kreckel, K., Santoro, F., et al. 2023, *MNRAS*, **520**, 4902  
 Guillochon, J., Parent, J., Kelley, L. Z., & Margutti, R. 2017, *ApJ*, **835**, 64  
 Hannon, S., Lee, J. C., Whitmore, B. C., et al. 2022, *MNRAS*, **512**, 1294  
 Harris, C. R., Millman, K. J., van der Walt, S. J., et al. 2020, *Natur*, **585**, 357  
 Humason, M. L., Kearns, C. E., & Gomes, A. M. 1962, *PASP*, **74**, 215  
 Hunter, J. D. 2007, *CSE*, **9**, 90  
 James, P. A., & Anderson, J. P. 2006, *A&A*, **453**, 57  
 Jha, S. W., Camacho, Y., Dettman, K., et al. 2017, *ATel*, **10640**, 1  
 Kasliwal, M. M., Sahu, D. K., & Anupama, G. C. 2009, *CBET*, **1874**, 2  
 Kawamura, A., Mizuno, Y., Minamidani, T., et al. 2009, *ApJS*, **184**, 1  
 Keller, B. W., & Kruijssen, J. M. D. 2022, *MNRAS*, **512**, 199  
 Kennicutt, R. C., & Evans, N. J. 2012, *ARA&A*, **50**, 531  
 Kim, C.-G., & Ostriker, E. C. 2015, *ApJ*, **802**, 99  
 Kim, J., Chevance, M., Kruijssen, J. M. D., et al. 2021, *MNRAS*, **504**, 487  
 Kim, J., Chevance, M., Kruijssen, J. M. D., et al. 2022, *MNRAS*, **516**, 3006  
 Kirshner, R., Schild, R., Wilson, I. R. G., Buta, R., & Meurer, G. 1985, *IAUC*, **4143**, 1  
 Klotz, A., Maury, A., Childress, M., et al. 2012, *CBET*, **3275**, 1  
 Kluver, T., Ragan-Kelley, B., Pérez, F., et al. 2016, *Positioning and Power in Academic Publishing: Players, Agents and Agendas* (Amsterdam: IOS Press), 87  
 Kochanek, C. S., Shappee, B. J., Stanek, K. Z., et al. 2017, *PASP*, **129**, 104502  
 Kruijssen, J. M. D. 2014, *CQGra*, **31**, 244006  
 Kruijssen, J. M. D., Schruha, A., Chevance, M., et al. 2019, *Natur*, **569**, 519  
 Kruijssen, J. M. D., Schruha, A., Hygate, A. P. S., et al. 2018, *MNRAS*, **479**, 1866  
 Kuncarayakti, H., Doi, M., Aldering, G., et al. 2013, *AJ*, **146**, 30  
 Lee, J. C., Whitmore, B. C., Thilker, D. A., et al. 2022, *ApJS*, **258**, 10  
 Leitherer, C., Ekström, S., Meynet, G., et al. 2014, *ApJS*, **212**, 14  
 Leitherer, C., Schaerer, D., Goldader, J. D., et al. 1999, *ApJS*, **123**, 3  
 Leonard, P. b. C., Pignata, G., Dessart, L., et al. 2013, *ATel*, **5275**, 1  
 Leroy, A. K., Sandstrom, K., Rosolowsky, E., et al. 2023, *ApJL*, **944**, L9  
 Leroy, A. K., Schinnerer, E., Hughes, A., et al. 2021, *ApJS*, **257**, 43  
 Li, L., Cai, Y., Zhai, Q., Zhang, J., & Wang, X. 2022, *TNSCR*, **2022-3549**, 1  
 Li, W., Leaman, J., Chornock, R., et al. 2011, *MNRAS*, **412**, 1441  
 Lockman, F. J. 1989, *ApJS*, **71**, 469  
 Lopez, L. A., Krumholz, M. R., Bolatto, A. D., et al. 2014, *ApJ*, **795**, 121  
 Maoz, D., Mannucci, F., & Nelemans, G. 2014, *ARA&A*, **52**, 107  
 Martizzi, D., Faucher-Giguère, C.-A., & Quataert, E. 2015, *MNRAS*, **450**, 504  
 Marvin, H., Perlmutter, S., Seal, D., et al. 1989, *IAUC*, **4727**, 1  
 Mayker Chen, N., Leroy, A. K., Lopez, L. A., et al. 2023, *ApJ*, **944**, 110  
 McKinney, W. 2010, in Proc. 9th Python in Science Conf., ed. S. van der Walt & J. Millman (Austin, TX: SciPy), 56  
 McLeod, A. F., Ali, A. A., Chevance, M., et al. 2021, *MNRAS*, **508**, 5425  
 McLeod, A. F., Dale, J. E., Evans, C. J., et al. 2019, *MNRAS*, **486**, 5263  
 McLeod, A. F., Kruijssen, J. M. D., Weisz, D. R., et al. 2020, *ApJ*, **891**, 25  
 Monard, L. A. G. 2008, *CBET*, **1315**, 1  
 Nguyen, C. T., Costa, G., Girardi, L., et al. 2022, *A&A*, **665**, A126  
 Ochner, P., Tomasella, L., Benetti, S., et al. 2014, *CBET*, **4011**, 2  
 O'Donnell, J. E. 1994, *ApJ*, **422**, 158  
 Olivier, G. M., Lopez, L. A., Rosen, A. L., et al. 2021, *ApJ*, **908**, 68  
 Ostriker, E. C., & Shetty, R. 2011, *ApJ*, **731**, 41  
 Pan, H.-A., Schinnerer, E., Hughes, A., et al. 2022, *ApJ*, **927**, 9

- Patton, R. A., Sukhbold, T., & Eldridge, J. J. 2022, *MNRAS*, 511, 903
- Pejcha, O., & Prieto, J. L. 2015, *ApJ*, 799, 215
- Pennypacker, C., Burns, S., Crawford, F., et al. 1986, *IAUC*, 4219, 1
- Perley, D., Barbarino, C., Sollerman, J., et al. 2020, *TNSAN*, 100, 1
- Pessa, I., Schinnerer, E., Belfiore, F., et al. 2021, *A&A*, 650, A134
- Pessi, T., Prieto, J. L., Anderson, J. P., et al. 2023, *A&A*, 677, A28
- Pignata, G., Maza, J., Hamuy, M., et al. 2009, *CBET*, 1902, 1
- Pilyugin, L. S., & Grebel, E. K. 2016, *MNRAS*, 457, 3678
- Pokhrel, N. R., Simpson, C. E., & Bagetakos, I. 2020, *AJ*, 160, 66
- Porter, A. C. 1993, *PASP*, 105, 1250
- Pritchett, C., Thanjavur, K., Bottrell, C., & Gao, Y. 2024, arXiv:2401.13826
- Querejeta, M., Schinnerer, E., Meidt, S., et al. 2021, *A&A*, 656, A133
- Quimby, R., Brown, P., Gerardy, C., Odewahn, S. C., & Rostopchin, S. 2006, *CBET*, 393, 1
- Rahner, D., Pellegrini, E. W., Glover, S. C. O., & Klessen, R. S. 2017, *MNRAS*, 470, 4453
- Rosino, L. 1972, *IAUC*, 2472, 1
- Sanders, D. B., & Mirabel, I. F. 1996, *ARA&A*, 34, 749
- Santoro, F., Kreckel, K., Belfiore, F., et al. 2022, *A&A*, 658, A188
- Sarbadhicary, S. K., Wagner, J., Koch, E. W., et al. 2023, arXiv:2310.17694
- Schinnerer, E., Hughes, A., Leroy, A., et al. 2019, *ApJ*, 887, 49
- Schruba, A., Leroy, A. K., Walter, F., Sandstrom, K., & Rosolowsky, E. 2010, *ApJ*, 722, 1699
- Shappee, B. J., Prieto, J. L., Grupe, D., et al. 2014, *ApJ*, 788, 48
- Sheth, K., Regan, M., Hinz, J. L., et al. 2010, *PASP*, 122, 1397
- Siebert, M., & Foley, R. 2022, *TNSCR*, 2022-170, 1
- Siebert, M. R., Kilpatrick, C. D., Foley, R. J., & Cartier, R. 2020, *ATel*, 13393, 1
- Smartt, S. J. 2009, *ARA&A*, 47, 63
- Smartt, S. J., Kilkenny, D., & Meikle, P. 2001, *IAUC*, 7704, 1
- Sukhbold, T., Ertl, T., Woosley, S. E., Brown, J. M., & Janka, H. T. 2016, *ApJ*, 821, 38
- Thilker, D. A., Braun, R., & Walterbos, R. A. M. 2000, *AJ*, 120, 3070
- Tsvetkov, D. Y., & Bartunov, O. S. 1993, *BICDS*, 42, 17
- Valenti, S., Sand, D. J., Wyatt, S., et al. 2021, Transient Name Server Discovery Report, 2021-633
- van der Walt, S., Colbert, S. C., & Varoquaux, G. 2011, *CSE*, 13, 22
- van Dyk, S. D., Hamuy, M., & Filippenko, A. V. 1996, *AJ*, 111, 2017
- Vartanyan, D., Laplace, E., Renzo, M., et al. 2021, *ApJL*, 916, L5
- Veilleux, S., Maiolino, R., Bolatto, A. D., & Aalto, S. 2020, *A&ARv*, 28, 2
- Virtanen, P., Gommers, R., Oliphant, T. E., et al. 2020, *NatMe*, 17, 261
- Walch, S., Girichidis, P., Naab, T., et al. 2015, *MNRAS*, 454, 238
- Waskom, M., Botvinnik, O., O’Kane, D., et al. 2017, mwaskom/seaborn: v0.8.1 (2017 September), v.v0.8.1, Zenodo, doi:10.5281/zenodo.883859
- Watkins, E. J., Barnes, A. T., Henny, K., et al. 2023a, *ApJL*, 944, L24
- Watkins, E. J., Kreckel, K., Groves, B., et al. 2023b, *A&A*, 676, A67
- Wheeler, J. C., Harkness, R. P., Barker, E. S., Cochran, A. L., & Wills, D. 1987, *ApJL*, 313, L69
- Yamaoka, H., Itagaki, K., Guido, E., et al. 2014, *CBET*, 3795, 2
- Zapartas, E., de Mink, S. E., Izzard, R. G., et al. 2017, *A&A*, 601, A29
- Zhang, J., Zheng, X., Wang, X., & Rui, L. 2016, *ATel*, 9093, 1